Internal report 98/1
PiP/TOF

Analytical Treatment of Coherent Bremsstrahlung

F. A. Natter
natter@pit.physik.uni-tuebingen.de

Physikalisches Institut
der Universität Tübingen
Auf der Morgenstelle 14
D-72076 TÜBINGEN
GERMANY

Dez 1998

Contents

List of Figures

List of Tables

1 Introduction

Polarised photon beams are quite important because asymmetries are much more sensitive to some variables than are absolute cross sections. This originates from the linear dependence of the asymmetry on these variables, which otherwise enter the cross section quadratically. Another advantage lies in the cancellation of dominant processes, which are already known from absolute measurements.

In spring 1996 a $^4\mathrm{He}(\vec{\gamma}, \mathrm{NN})$ experiment was performed at MAMI and it is of vital importance for the analysis to extract the polarisation of the photon beam. Here, the only possible access to this observable is based on a derivation from the measured bremsstrahlung spectra.

1.1 Kinematics

When considering the bremsstrahlung process one has to deal first with the kinematics. This is shown in figure 1, with the equations respecting energy and momentum conservation. During these experiments photons in the energy range of 100–350 MeV had been produced by 855 MeV electrons. This allowed the neglection of recoil energy T in kinematical calculations. Due

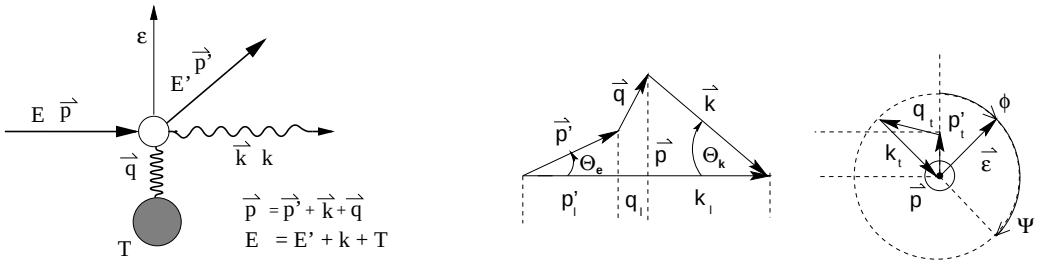

Figure 1: *Left: kinematics of the bremsstrahlungs process and the notation of energies and momenta involved. Right: Longitudinal and transversal momentum decomposition (not to scale).*

to energy and momentum conservation an ansatz for decomposition of the momenta in longitudinal and transversal components leads to constraints of the recoil momentum. The longitudinal momentum is much smaller than the transverse one allowing a very shallow region with respect to the incident electron momentum, which is called pancake; its limits depend only, on $x = k/E$, the relative photon energy. This holds for every single bremsstrahlungs process, but employing a lattice as radiator introduces additional constraints

[fig. 2]. Coherent scattering with corresponding bremsstrahlung is only possible if the so called Bragg condition is satisfied. This requires that the recoil momentum $\vec{q}$ coincides with a reciprocal lattice vector $\vec{g}$, or in other words, $\vec{g}$ must lie inside the pancake. The consequences for the bremsstrahlungs spectrum and the photon properties are discussed in the following section.

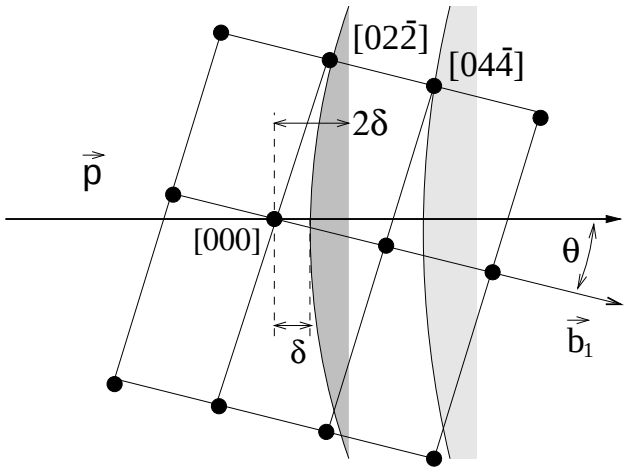

Figure 2: *Pancakes in reciprocal lattice space of diamond for two different photon energies.* $\delta = \frac{m_e^2}{2E}\frac{1}{1-x}$ *denotes the minimum longitudinal momentum transfer and* θ *the crystal angel between the incident electron momentum and basis vector* $\vec{b}_1$.

1.2 Elementary process

The purpose of this section is to sketch the underlying QED process of the bremsstrahlung and to derive the qualitative behaviour of the cross section particularly concerning the polarisation properties of the photon beam. Due to energy and momentum conservation a free electron is not able to emit a photon, but a third partner (i.e. atom) is needed which absorbs the appropriate transfer momentum [fig. 1]. This takes place via an exchange of a virtual photon, which turns bremsstrahlung to a second order process in the QED coupling constant. The corresponding Feynman graph is sketched in figure 3, while the reverse time ordering – first photon emission and then interaction with a coulomb potential – contributes, too. With the help of the Feynman rules, see for example [Hal84, Bjø64], the invariant amplitude in momentum space, whose squared value is proportional to the cross section,

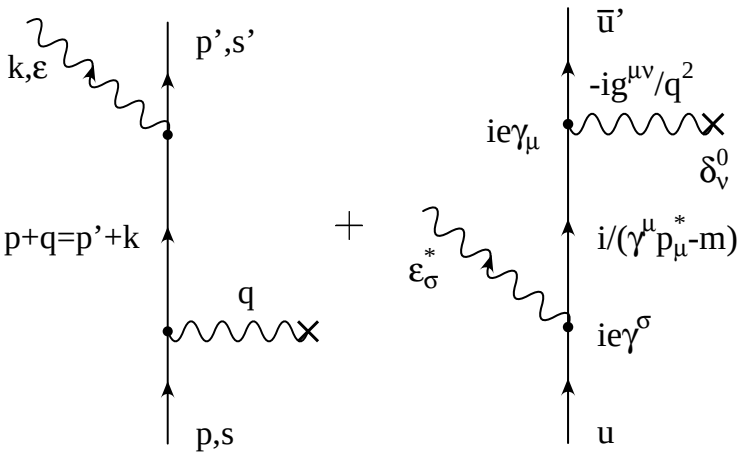

Figure 3: *Left: Feynman-graph in lowest order of the bremsstrahlung process with momenta. Right: Time reversed graph with propagators and vertex factors*

can be written as (the invovled symbols are defined in figure 3) :

$$\mathcal{M} \propto \frac{1}{\sqrt{2k}\vec{q}^2}\bar{u}(p',s')\left[\not{\epsilon}\frac{1}{\not{p}'+\not{k}-m}\gamma_0+\gamma_0\frac{1}{\not{p}'-\not{k}-m}\not{\epsilon}\right]u(p,s) \qquad (1)$$

At a vertex where the emission of a free photon with polarisation ϵ_μ takes place a factor of $-i\not{\epsilon}/\sqrt{2k}$ has to be applied. This stems from the plane wave of the electromagnetic four-potential, which is attached to a "photon" : $A_\mu = \epsilon_\mu/\sqrt{2k}\cdot(e^{-ik\cdot x}+e^{ik\cdot x})$. Constraints for the polarisation vector arise from the Maxwell equations and the gauge freedom: $\epsilon \cdot k = 0$ (meaning that real photons are transverse) and $\epsilon_\mu^2 = -1$. The first term of A_μ will be neglected, because it describes a photon absorption from the quantum field and is not observed here. The interaction with an outer static Coulomb field $A_\mu = \delta_{\mu 0}\cdot(-Ze/4\pi|\vec{x}|)$ is described by a factor of $-i\not{A}$. Expanding the first term in (1) with $\not{p}'+\not{k}+m$ and considering $\{\not{a},\not{b}\} = 2a\cdot b$ leads to $\not{\epsilon}\frac{\not{p}'+\not{k}+m}{(p'+k)^2-m^2}\gamma_0$. Since only the main features of the cross section shall be derived here, the further calculation is limited to soft photon emission ($k \to 0$), which facilitates the algebra. If the properties of the Dirac spinors are used and terms linear in k are neglected the first term in (1) becomes: $\bar{u}(p')\frac{-(\not{p}'-m)\not{\epsilon}+2p'\cdot\epsilon}{2p\cdot k}\gamma_0 = \bar{u}'\frac{p'\cdot\epsilon}{p'\cdot k}\gamma_0$ and thus the invariant amplitude, omitting the phase space factor for sake of convenience, reads:

$$\mathcal{M} \propto \bar{u}'\gamma_0 u\left(\frac{\epsilon\cdot p'}{k\cdot p'}-\frac{\epsilon\cdot p}{k\cdot p}\right) \qquad (2)$$

The first factor in equation (2) leads to the elastic cross section (key word 'Rutherford scattering'), which is well known and shall not be presented here. The resulting so called Bethe-Heitler cross section in the soft photon approximation without the usual summation over the photon polarisations, which are given here in the coulomb gauge ($\epsilon_0 = 0$), reads:

$$\frac{d\sigma}{dk\, d\Omega_k\, d\Omega_e} = \sigma^{\mathrm{e}}_{\mathrm{elast}} \times \frac{e^2 k}{2(2\pi)^3} \left(\frac{\vec{\epsilon}\vec{p}'}{k \cdot p'} - \frac{\vec{\epsilon}\vec{p}}{k \cdot p} \right)^2 \Theta(E - k - m) \qquad (3)$$

In order to see the dependence of the cross section on the polarisation a special kinematic, employed in the setup of the ^{4}He$(\vec{\gamma}, \mathrm{NN})$ experiments in 1996, is considered in the following: $\vec{p} \,||\, \vec{k} \,||\, \vec{e}_x$ ($\vec{e}_x$ being the basis vector along the x-axis of the lab system, i.e. the incoming electron). After integration of (3) over the electron emission angles the dependence on photon energy and polarisation, where ϕ denotes the angle between the polarisation vector $\vec{\epsilon}$ and the scattering plane $\vec{p}, \vec{p}'$ [fig. 1], is easily noticed:

$$\frac{d\sigma}{dk} \propto \frac{1}{k} \cos^2 \phi \qquad (4)$$

One sees, that the cross section drops in leading order with $1/k$ and that polarisation vectors, which lie in the electron scattering plane, contribute most strongly, producing a photon polarisation $P = (\sigma_\perp - \sigma_{||})/(\sigma_\perp + \sigma_{||})$ of unity.

If we consider photons emitted along the incident electron momentum only (i.e z-axis) the scattering plane is determined due to momentum conservation [fig. 1] by the recoil momentum $\vec{q}$. In the case of incoherent bremsstrahlung, which means scattering off amorphous material or off one single atom respectively, the recoil momentum is isotropically distributed around the z-axis consequently leading to an unpolarised photon beam. However, if the recoil momentum is fixed most of the photons have the same polarisation vector due to equation (4) yielding a polarised beam. In comparison to the restricted case considered here, a non vanishing photon beam divergence reduces the polarisation. The broader the angular distribution the smaller the integral polarisation turns out to be. This "scattering plane fixing" occurs when a lattice is used as a radiator, because then the recoil is not transfered to a single atom but to the lattice, which constrains the recoil via the Bragg condition: $\vec{q} = \vec{g}_{hkl}$ figure 2. Only recoil momenta which coincide with a reciprocal lattice vector, defined by the Miller indices [hkl], contribute to the coherent bremsstrahlung cross section. The second constraint is due to the so called pancake [fig. 2], which allows the selection of a photon energy range and of just one or a small subset of reciprocal lattice vectors g_{hkl} via appropriate rotations of the crystal.

2 Cross section and polarisation

2.1 Ideal electron beam without photon collimation

The elaborate treatment by May [Tim69, May51] leads to the five fold differential cross section, which is reduced by integration over the photon and electron angles [Bol62, Dia68] and used in the following analytical calculations. Formulas may also be found in [Ram95, Loh94] with a more detailed discussion:

$$d\sigma = [f D(\vec{q}) + (1-f)N]\, F^2 d\sigma^{\text{coul}} = d\sigma^{\text{coh}} + d\sigma^{\text{inc}} \tag{5}$$

Here, in the total cross section $d\sigma/dk$ of a crystal, the diffraction factor D describes the influence of the crystal structure, whereas the formfactor F models the atomic structure, i.e. the charge distribution. The so called Debye-Waller factor, $\exp(-A(T)q^2) = f(q^2) \in [0,1]$, which depends on the temperature T, determines the ratio of coherent to incoherent cross section, which takes place on $(1-f)N$ Atoms. The cross sections of the coherent ($\sigma_{\text{coh}} = \sigma_\perp + \sigma_\parallel$) and incoherent ($\sigma_{\text{inc}}$) part, the latter corrected for contributions of scattering off the shell electrons in the crystal, and the resulting polarisation (all in terms of functions Ψ_i) used for the calculation read in common notation:

$$I^{\text{coh/inc}} = \frac{x}{\bar{\sigma}} \frac{d\sigma^{\text{coh/inc}}}{dx} = (1 + (1-x)^2)\Psi_1^{\text{coh/inc}} - \frac{2}{3}(1-x)\Psi_2^{\text{coh/inc}} \tag{6}$$

$$\text{with} \quad \Psi_1^{\text{el}} = 4.05 \qquad \Psi_2^{\text{el}} = 3.94 \tag{7a}$$

$$\Psi_1^{\text{inc}} = 4 + 4\int_\delta^1 q dq\,(1-f)F^2(q-\delta)^2 \approx 13.3 \tag{7b}$$

$$\Psi_2^{\text{inc}} = \frac{10}{3} + 4\int_\delta^1 q dq\,(1-f)F^2\left(q^2 - \delta^2\left(\ln\frac{q}{\delta} - 4\frac{\delta}{q} + 3\right)\right) \approx 12.6$$

$$\begin{aligned} \Psi_1^{\text{coh}} &= 4\sum\nolimits_{\vec{g}} G\delta g_t^2 g_l^2 \\ \Psi_2^{\text{coh}} &= 24\sum\nolimits_{\vec{g}} G\delta^2 (g_l - \delta) g_t^2 \\ \Psi_3^{\text{coh}} &= -4\sum\nolimits_{\vec{g}} G\delta^3 [(g_2^2 - g_3^2)\cos 2\phi + 2 g_2 g_3 \sin 2\phi] \end{aligned} \tag{8a}$$

$$\begin{aligned} \text{and} \quad G(\vec{g}) &= (2\pi)^2 a^{-3} S^2(\vec{g}) e^{-Ag^2} F^2(g^2) g^{-4} g_l^{-4} \\ g_t^2 &= g_2^2 + g_3^2 + \sin^2\theta (g_1^2 - (g_2\cos\alpha + g_3 \sin\alpha)^2) \\ g_l &= g_1 \cos\theta + \sin\theta (g_2 \cos\alpha + g_3 \sin\alpha)) \end{aligned} \tag{8b}$$

Here the lattice vectors enter via $|\vec{g}| = |\sum g_i \vec{b}_i| = g$ and $g_l = \delta(x_d) > \delta(x) = \frac{1}{2E_0}\frac{x}{1-x}$ with $E_0 = 1673$ beeing the electron energy as provided from MAMI in units of the electron mass. For maximum polarisation the angle ϕ (4) between polarisation vector and a reference plane was chosen to $\tan\phi = g_3/g_2$ of the $[02\bar{2}]$ lattice vector. For the incoherent description the atomic form-factor $F(q^2)$ and the Debye Waller factor is taken into account via equation (7b), compare (4BSb) in [KoM59], and is further denoted as Bethe Heitler intensity (BH). The cross sections, intensities and polarisations were calculated in the program ANB in the language C and part of the code is presented in the following:

```
#define EPS      -0.78539816
#define GUNIT    M_2PI/923.7
#define X_RANGE  1000.
#define E0       855./MASS_ELECTRON

void int_coh( double *intsum, double *intdif )
{
  for( l=0; l<max_latticevec; l++ )  /* loop over lattice-vecs lv[] */
  {
  g     = lv[l];
  g_2   = v_sprd( g, g ) * GUNIT*GUNIT;
  aps   = ((g.y*g.y-g.z*g.z)*cos(2*EPS)+2*g.y*g.z*sin(2*EPS))*GUNIT*GUNIT;
  ff    = 0.2283 + 1.8359*exp(-10528*g_2) + 1.8119*exp(-4678*g_2)
        + 1.5809*exp(-239*g_2) + 0.5426*exp(-27116*g_2);
  ff    = 1.-ff/6.;
  dmy   = sin(theta) * ( g.y*cos(alpha) + g.z*sin(alpha) );
  gl    = ( cos(theta)*g.x + dmy ) * GUNIT;
  gt_2  = (g.y*g.y+g.z*g.z+pow(sin(theta)*g.x,2.)-dmy*dmy)*GUNIT*GUNIT;
  xd    = 2.*E0*gl / ( 1. + 2.*E0*gl );
  dmy   = M_2PI*ff / (g_2*gl*gl);
  Gg    = A3/8.  * dmy*dmy * S_2[l] * exp(-Adebye*g_2);

  for( i=1; i<=X_RANGE; i++ )       /* loop over all photon energies */
  {  x    = (double)i/X_RANGE;
     if( x>xd ) {  i=X_RANGE; continue;  }
     del = x/(2.*E0*(1.-x));
     psi1 =  4 * Gg * del * gt_2 * gl*gl;  /* calc psi - fcts  */
     psi2 = 24 * Gg * del*del * gt_2 * (gl-del);
     psi3 = -4 * Gg * del*del*del * aps;         /* calc intensities */
     intsum[i] += ( (1.+(1.-x)*(1.-x))*psi1 - 2./3.*(1.-x)*psi2 )
     intdif[i] -= 2*(1.-x)*psi3;  }
  }
}
```

The functions Ψ_i^{coh} computed by this program are presented in figure 4, and the resulting cross sections and intensities are plotted in figure 5. The co-

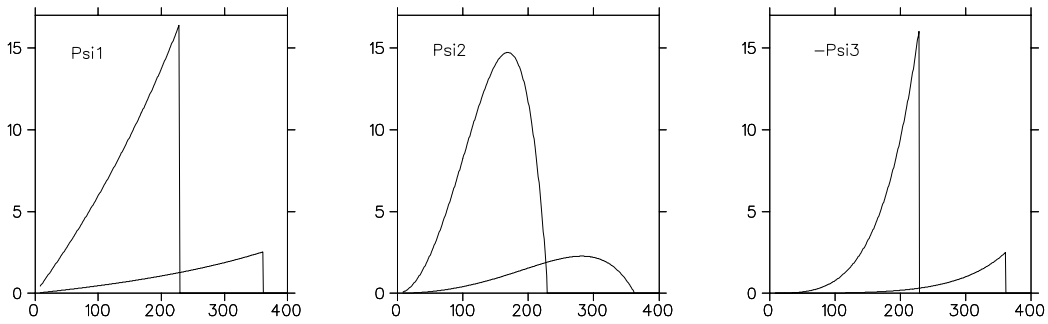

Figure 4: *Functions* Ψ_i^{coh} *versus photon energy in MeV for lattice vectors* $[02\bar{2}]$ *and* $[04\bar{4}]$.

herent (lattice vectors $[02\bar{2}]$ and $[04\bar{4}]$ only) and incoherent part in units of $\bar{\sigma} = 0.57947 \cdot Z^2$mb versus photon energy in MeV are shown as well as the sum of both and the relative intensity. Due to the definition of the intensity $I(x) = x\sigma(x)/\bar{\sigma}$ the relative intensity $I_{\mathrm{rel}} = (I_{\mathrm{coh}} + I_{\mathrm{inc}})/I_{\mathrm{inc}}$, and the relative cross section are identical. The comparison of the absolute and relative cross section with the measured yields, obtained with a nickel and a diamond radiator without collimation, may be seen in figure 6. The yield from nickel and diamond were each normalized in the energy range of 50 to 500 MeV on the analytical incoherent and total cross section, (7,8). The

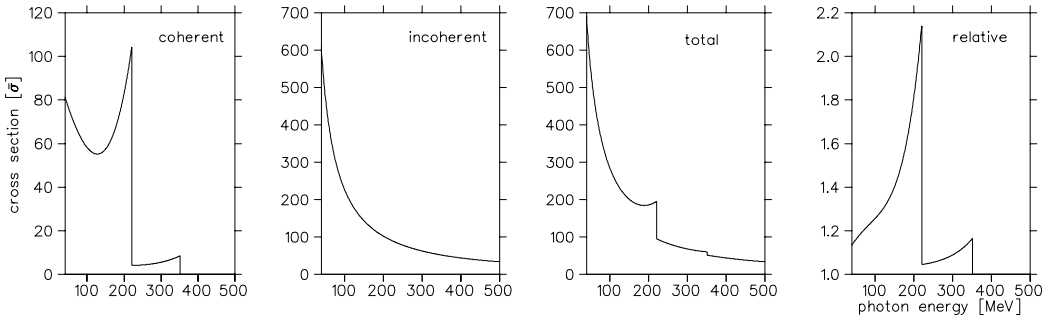

Figure 5: *Analytical calculated absolute and relative cross sections and intensity in units of* $\bar{\sigma} = 0.57947 \cdot Z^2 mb$

overall agreement is quite good although the analytical description does not take into account effects which stem from multiple scattering, electron beam divergence and collimation. These spectra may also be used for a comparison with the Monte Carlo program MCB [fig. 7], which is presented in [Wun97], in order to check its results. These formulas can be used for a proper normalisation of the experimental spectra as well as the ones simulated by MCB to the analytical cross sections. For the comparison of the measured and simulated

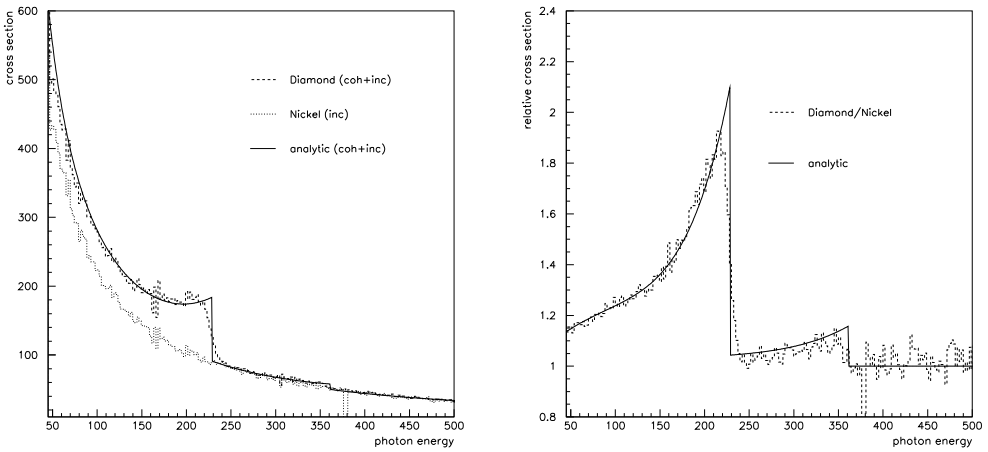

Figure 6: *Comparison of absolute (left in units of $\bar{\sigma}$) and relative (right in arbitrary units) cross sections with the experimental yields (note: $\sigma_{\mathrm{rel}} = I_{\mathrm{rel}}$), which are normalised on the absolute analytical cross section via the integrals in the range of 50 to 500 MeV. This fixes the normalisation factor for the relative experimental spectrum.*

relative intensity, the correct normalisation is of vital importance. In order to obtain the uncollimated polarisation, the following formulas [Ram95, Loh94] were applied for the polarisation presented in figure 6 and 8, where $d\sigma$ is an abbrevation of the single differential cross section $d\sigma/dk$ integrated over photon and electron angles.

$$P = \frac{d\sigma_{\perp}^{\mathrm{coh}} - d\sigma_{\parallel}^{\mathrm{coh}}}{d\sigma^{\mathrm{coh}} + d\sigma^{\mathrm{inc}}} = \frac{2(1-x)\Psi_3^{\mathrm{coh}}}{I_{\mathrm{tot}}} \tag{9a}$$

$$\text{with} \quad \Psi_{1/2/3}^{\mathrm{coh}} \overset{(8a)}{=} \sum\nolimits_{\vec{g}} \Psi_{1/2/3}^{\mathrm{coh}}(\vec{g})$$

$$I_{\mathrm{tot}} \overset{(6)}{=} I_{\mathrm{inc}} + \sum\nolimits_{\vec{g}} I_{\mathrm{coh}}(\vec{g}) \tag{9b}$$

Therefore the polarisation is a ratio over sums from contributions of different lattice vectors and may not be expressed as a sum over polarisations from different lattice vectors. The consequence of this is firstly, that due to $\Psi_3^{\mathrm{coh}}(\vec{g})$ beeing smaller than $I_{\mathrm{coh}}(\vec{g})$ the polarisation of one lattice vector only is higher than the resulting polarisation, considering the additional contributions of higher lattice vectors. Secondly, the analytical step from equation (5.17) in [Ram95] (9a here) to equation (5.30) is only possible if just one lattice vector is considered, but is no longer valid if higher lattice vectors

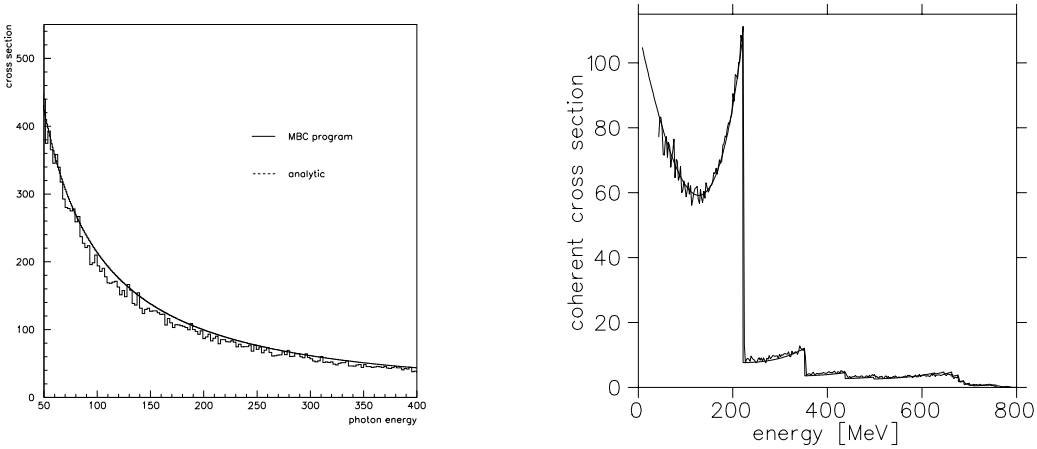

Figure 7: *Comparison of uncollimated MCB yield for ideal case and 15 lattice vectors (see text) and normalisation (via integration over plotted energy range) on the analytical cross section in units of $\bar{\sigma}$ versus photon energy in MeV*

contribute as well. For example the evaluation at the edge $x_d(220\text{MeV})$ results in $P = 50.0\%$ from lattice vector $[02\bar{2}]$, and $P = 1.9\%$ from $[04\bar{4}]$; both give a polarisation of 49.8% which is smaller than the one from the main contributing vector! The total polarisation distribution for two lattice vectors, combined and single, produced by ANB via (9a) is shown in figure 9 and may be compared with the simulations from Rambo's code and MCB for the ideal case without collimator. In order to check the influence of higher lattice vectors, and to ensure the correct treatment of 'adding' the contributions from different lattice vectors, the comparison between analytical results and MCB was done for fifteen lattice vectors, which amount to almost the total cross section, and are presented in figure 8. The lattice vectors used in this calculation and additional fiffteen are shown in table 1, sorted in descending order according their relative contribution.

2.2 Ideal electron beam and photon collimation

The influence of a finite beam spot size, transversal beam momentum distribution, and multiple scattering is the typical domain of a Monte Carlo treatment, but the analytically calculation of collimation effects is feasible and is presented in the following. Due to kinematical constraints for a given lattice vector and photon energy the photon emission angles are not independent from each other, but the polar angle ϑ_k is a function of the azimuthal

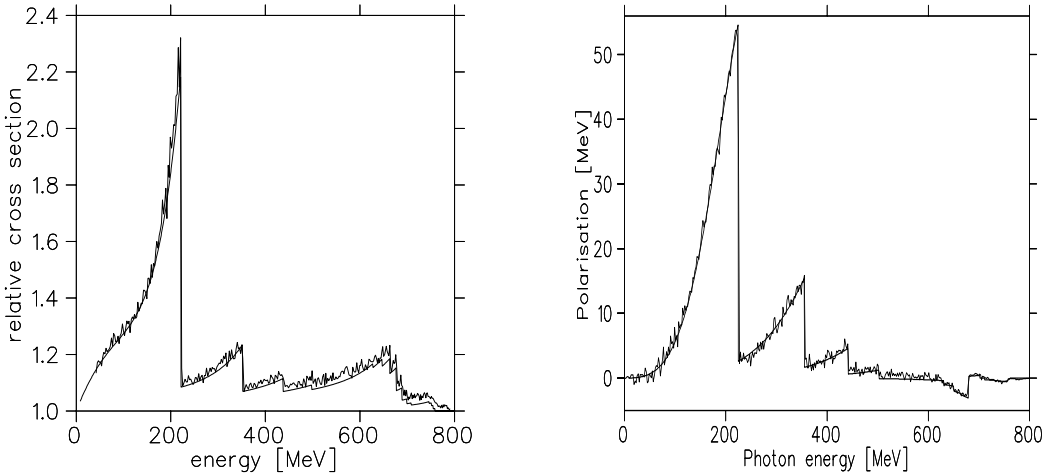

Figure 8: *Comparison of the analytical calculation, using 15 lattice vectors (see text), to MCB polarisation (left) and relative cross section (right). The energy of the discontinuity (edge) due to vector* $[02\bar{2}]$ *is at* $x_d(\theta = 0.0607\,\mathrm{mrad}, \alpha = 0.694\,\mathrm{mrad}) = 220\ MeV$

one (ψ_1).

$$U(\psi_1) = \vartheta_k E_0 = \Gamma(\psi_1) + \sqrt{\Gamma^2 + \frac{g_l}{\delta} - \frac{g_t^2}{x} - 1} \tag{10a}$$

$$\text{with} \quad \Gamma(\psi_1) = -g_2 \cos(\psi_1 - \alpha) + g_3 \sin(\psi_1 - \alpha) \tag{10b}$$

This photon energy dependence of the polar angle has to be accounted for in the triple differential cross section via Dirac's delta distribution δ^D using $u = U^2$:

$$I_\Omega^{\mathrm{coh}} = \left[(1 + (1-x)^2)\Phi_1 - \frac{2}{3}(1-x)\Phi_2\right] \delta^D(u - u(\psi_1))\, du\, d\psi_1 \tag{11}$$

$$P_\Omega I^{\mathrm{tot}} = 2(1-x)\Phi_4(\psi_1)\delta^D(u - u(\psi_1))\, du\, d\psi_1 \tag{12}$$

The Φ functions shall not be presented here, but may be found elsewhere [Tim69], because all one needs to know is their relation to the Ψ functions: $\Psi_{1/2/3} = \int d\psi_1\, \Phi_{1/2/4}$. Now the effect of collimation is trivial: due to the δ^D distribution one detains a condition in terms of the collimator angle u_c for the contributions to the angle integral:

$$I_c = \int du\, d\psi_1 \frac{d^2 I_\Omega^{\mathrm{coh}}}{du\, d\psi_1} = \int_0^{u_c} du\, I^{\mathrm{coh}} \delta^D(u - u(x)) \overset{(15)}{=} I^{\mathrm{coh}}(x)\Theta(x - x_c) \tag{13}$$

I_{coh}	vector	k_d	S^2	I_{coh}	vector	k_d	S^2	I_{coh}	vector	k_d	S^2
26.4	[0, 2,-2]	225	64	0.24	[0, 4, 4]	758	64	0.14	[2,-2, 0]	836	64
3.54	[0, 4,-4]	356	64	0.21	[0, 2, 6]	753	64	0.13	[0, 0, 8]	749	64
1.63	[0, 2, 2]	680	64	0.21	[1,-1,-1]	816	32	0.13	[0,10,-10]	548	64
1.07	[0, 0, 4]	666	64	0.19	[0, 6, 2]	761	64	0.13	[1,-1,-3]	812	32
0.94	[0, 6,-6]	442	64	0.19	[1, 1,-1]	819	32	0.13	[1,-3,-1]	811	32
0.88	[0, 4, 0]	692	64	0.19	[1,-1, 1]	819	32	0.13	[2, 0, 2]	837	64
0.50	[0,-2, 6]	650	64	0.18	[1, 1, 1]	822	32	0.13	[2, 2, 0]	837	64
0.34	[0, 6,-2]	702	64	0.16	[0,-6,10]	608	64	0.12	[1, 1,-3]	816	32
0.33	[0, 8,-8]	503	64	0.15	[0, 8,-4]	711	64	0.12	[1,-3, 1]	815	32
0.27	[0,-4, 8]	631	6	0.14	[2, 0,-2]	836	64	0.11	[0, 8, 0]	765	64

Table 1: *Lattice vectors* $\vec{g} = (h, k, l) \cdot 2\pi/a$ *with diamond lattice spacing* a *used in the analytical calculation. The coherent intensities at the edges* k_d *for* $\alpha = 0.694, \theta = 0.0607$ *rad and the structure functions are recorded.*

Considering the order of magnitudes of the involved variables, the g_t^2/x term may be neglected compared to g_l/δ and the weak dependence on ψ_1 ($\Gamma \ll g_l/\delta$) justifies the approximation which was used for the ψ_1 integration in equation (13):

$$u(x, \psi_1) \approx u(x) = g_l/\delta(x) - 1 \tag{14}$$

Hence, if $u(x) < u_c$ the coherent cross section vanishes. Solving this condition for x, and rewriting it using the variable x_d instead of g_l, yields:

$$x_c = \frac{x_d}{1 + u_c(1 - x_d)} \tag{15}$$

Therefore, the only effect of collimation on the coherent side is a vanishing contribution below a certain photon energy x_c, which is the result of the constraint relation (10).

The effect of the collimation for the incoherent part does not affect the energy dependence of the cross section, but directly affects the angular one ($d^2\sigma^{\mathrm{inc}}/du \approx (1+u)^{-2}$) . Now the treatment of collimation just means in lowest approximation the application of a reduction factor f_c to the cross section $d\sigma^{\mathrm{inc}}$ (πE_0 is approximated by infinity) with:

$$f_c = \int_0^{u_c} du\, d^2\sigma^{\mathrm{inc}} \Big/ \int_0^{\infty} du\, d^2\sigma^{\mathrm{inc}} = \frac{u_c}{1 + u_c} \tag{16}$$

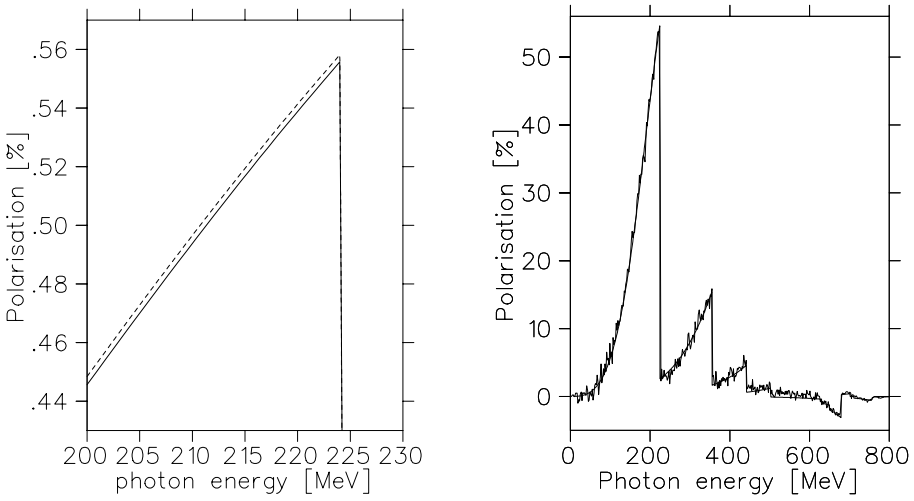

Figure 9: *Left: analytical polarisation for ideal case without collimator. Plotted are the polarisation amounting from two lattice vectors together and the ones from each vector alone. Right: comparison between MCB polarisation and the analytical one.*

For the applied collimation in the ^{4}He experiment of $\vartheta_c = 0.031°$, the polarisation for a diamond setting with discontinuity at 220 MeV may be seen in figure 10; and the relative spectra compared with the experimental ones. Remind that experimental insufficiencies, the effects mentioned above and treated in MCB , reduce the polarisation. This is the main reason for the bad description of the data, and proves the need for a Monte Carlo treatment, which is able to account for all these experimental effects. The analytical cross section does not show the blur on the edges like the experimental spectra, which are mainly due to transversal beam momentum distribution and multiple scattering as is demonstrated with MCB in [Wun97] and is modelled later on page 21. The sharp cutoff at low energies, which is caused by the collimator, entails that contributions from higher lattice vectors do not add to lower ones in the relative spectra, e.g. see the two lowest peaks in figure 10 left. This causes the discrepancy at higher photon energies in these spectra which is not the case for uncollimated yields and explains the good agreement there. The obvious discrepancy at low energies (the relative intensity beeing lower than unity) is not as serious as one might assume. It arises from two sources: an insufficent analytical description of the nickel and diamond incoherent intensity, and from different behaviour of those experimental yields at low energies. The nickel yield rises way steeper for E_γ as the diamond one leading to a collimated relative spectra which does not tend to unity at low photon energies [fig. 10] and leads also to a bad description in the uncol-

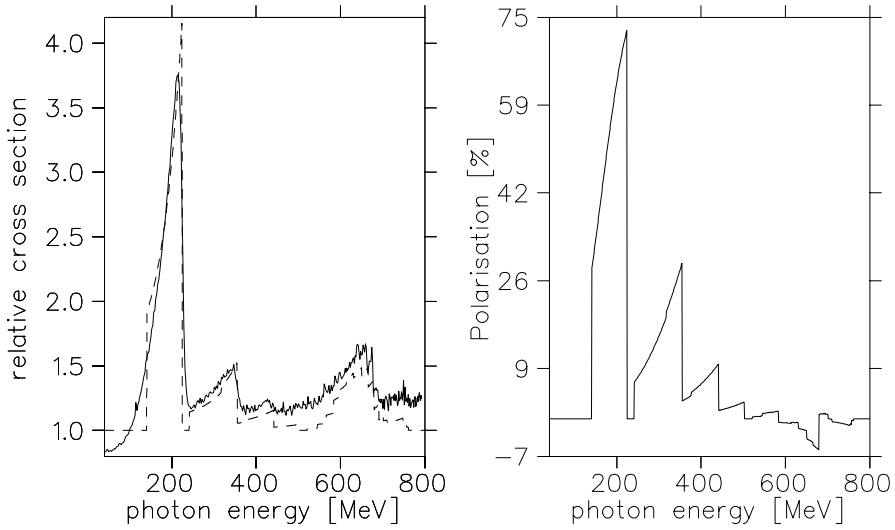

Figure 10: *Relative cross section, calculated (BH) for an ideal beam, is compared to the experimental one (left) and polarisation (right) for edge 220 MeV*

limated case calculated via the Bethe Heitler intensity (BH), see figure 11. As long as this behaviour is not understood or modelled appropiately, the problems at low energies prevent a proper normalisation of the experimental yields causing unreliable results concerning the predicted polarisation.

3 Experimental effects and improved analytical description

3.1 Hubbell intensity and electron contribution

Due to the problems mentioned above, neccesary improvements especially better cross sections for the incoherent part were adopted:

1. More accurate treatment of the angular and Z dependence of the incoherent cross intensity to account for collimation and different radiators.
2. Z and k dependent shell-electron contribution to the bremsstrahlung.
3. Multihit correction of the tagger spectra for uncollimated yields.

4. Approximate treatment of beam divergence, multiple scattering and beam spot size to further benefit of the short running time of ANB .

Instead of the simple treatment of the incoherent contribution via the cross section in equation (8a) the photon angular ($U = \vartheta_k E_0$) and Z dependent Schiff cross section [Hub58] for the incoherent nuclear bremsstrahlung contribution is used from now on, because of the better angular description as it is shown in figure 13:

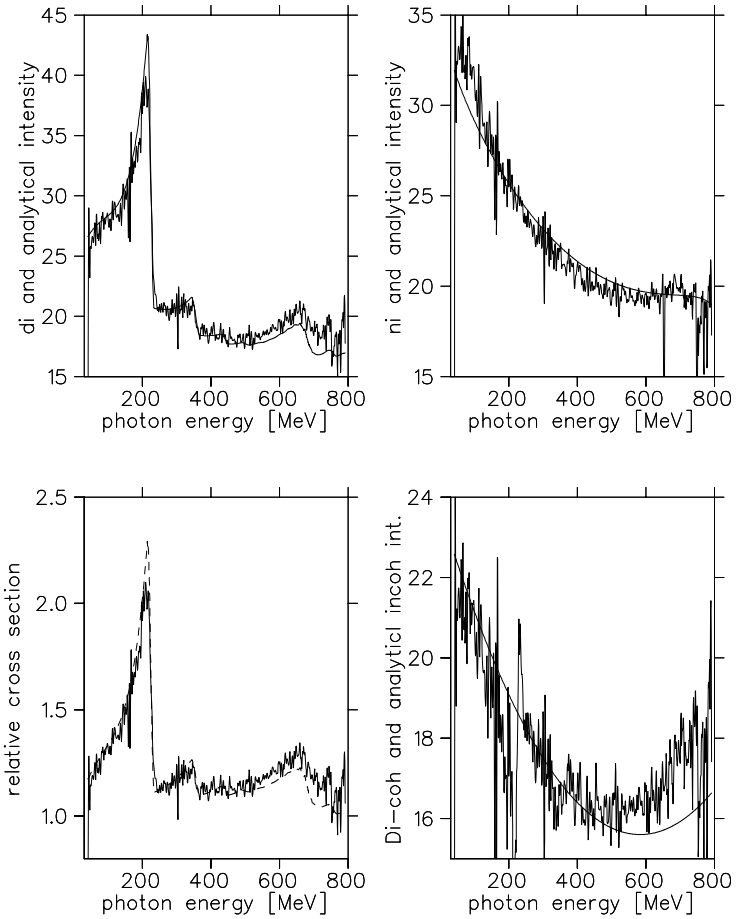

Figure 11: *Comparison between uncollimated analytical (BH) and experimental spectra. The lower right panel shows the differential spectrum (diamond subtracted by coherent intensity). The discrepancies proof again (see also page 16) the need for a better incoherent description.*

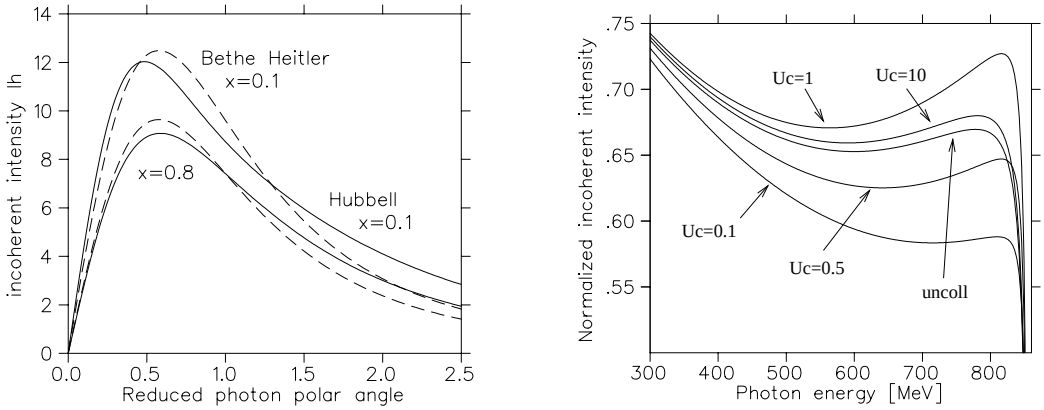

Figure 12: *Left: Bethe Heitler (page 15 and equation (8a)) and Hubbell intensity (17) dependence on the photon angle for different energies (x=0.1,0.8). Right: comparison of incoherent intensities from equation (18) for different collimation angles ($U_c = \vartheta_c E_0$). The intensities are normalized to one at the origin for ease of comparison.*

$$\begin{aligned}
\frac{dI}{UdU} &= (1+(1-x)^2)\Psi_1 - \frac{2}{3}(1-x)\Psi_2 \\
\Psi_1 &= 4v^2(M(v)-1) \\
\Psi_2 &= 12v^2(1+(2M(v)-8)(1-v)v) \\
\text{with} \quad M(v) &= -\ln\left[\left(\frac{x}{2E_0(1-x)}\right)^2 + \left(\frac{Z^{1/3}v}{C}\right)^2\right]
\end{aligned} \tag{17}$$

The integration of this cross section over the polar photon emission angle ϑ_k up to a limiting collimator angle $U_c = E_0\vartheta_c$ is feasible and presented here in terms of $v = (1+U_c^2)^{-1}$, see figure 12:

$$\begin{aligned}
\Psi_1 &= 2\left[1 + M(1) - (1+M(v))v - c\right] \\
\Psi_2 &= -\frac{40}{3}v^3 + 18v^2 - \left(\frac{8}{b^2}+6\right)v + \frac{8}{b^2} + \frac{4}{3} \\
&\quad + \left(4v^3 - 6v^2\right)M(v) + 2M(1) - \frac{6}{b^2}\left(M(v) - M(1) + \frac{2}{3}c\right) \\
\text{with} \quad c &= \frac{2}{b}\arctan\left(\frac{b(1-v)}{1+vb^2}\right) \qquad b = \frac{2Z^{1/3}E_0}{C}\frac{1-x}{x}
\end{aligned} \tag{18}$$

In equation (5) it is quantified how the incoherent contribution of a crystal radiatior is suppressed in comparison to an amorphous one. Therefore the

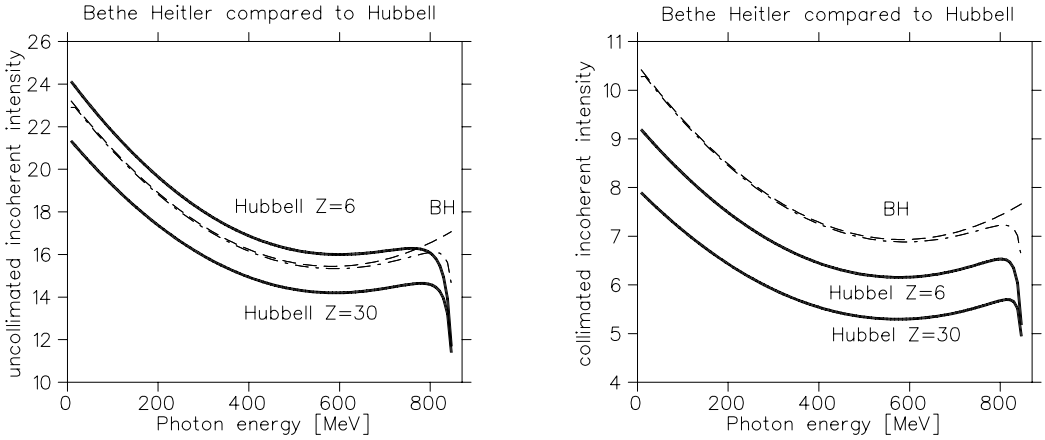

Figure 13: *Comparison of Z dependence of the incoherent intensities for collimated and uncollimated case. For the Bethe Heitler intensity $\psi(x)$ from equation (7b) and the constant values are plotted, whereas the angular reduction factor (16) was employed.*

Hubbell cross section, as stated in (17,18), may be used with the screening constant $C = 111$ from [Hub58] for amorphous radiators. Therein a Yukawa Potential, leading to a monopol formfactor of $F_C(q^2) = 1/(q^2 + (CZ^{-1/3})^2)$, was used to account for atoms with different Z. In case of a crystal a modified formfactor (see page 9) has to be applied: $F_{\mathrm{Deb}}(q^2) = F_C(q^2)(1 - f(q^2))$. Via a numerical comparison of $F_{C^{\mathrm{eff}}}$ and F_{Deb} an effective screening constant of $C^{\mathrm{eff}} = 32.2$ was evaluated and used to calculate the incoherent contribution of a crystal radiator.

From [KoM59] it is also possible to introduce a photon energy and Z dependence in the incoherent electron shell contribution which is adopted in the following. The discrepancy of (19,20) and (17) to the previous treatment is clearly seen figure 13 when compared with the Z and photon energy indepdend values used in (7):

$$\begin{aligned} \Psi_1^e &= Z^{-1}\left[\psi(\epsilon) - 4 - \frac{8}{3}\ln Z\right] \\ \Psi_2^e &= Z^{-1}\left[\psi(\epsilon) - \frac{10}{3} - \frac{8}{3}\ln Z\right] \qquad \text{with} \quad \epsilon = \frac{100}{E_0 Z^{2/3}}\frac{x}{1-x} \end{aligned} \tag{19}$$

The photon energy dependent function $\psi(\epsilon)$ is given in [MOw73] for different ϵ regions and corrected for binding effects and are repeated here for convenience (20). The resulting total intensities (integrated over the photon angle

$\int dE\ I(E)$	$I_{\mathrm{Ni}}^{\mathrm{inc}}$	$I_{\mathrm{Di}}^{\mathrm{inc}}$	$I_{\mathrm{Ni}}^{\mathrm{el}}$	$I_{\mathrm{Di}}^{\mathrm{el}}$	I^{coh}
Uncoll.	13844	11564	478	2751	3468
Coll.	5074	4001	213	1226	1521

Table 2: *Total intensities for the incoherent bremsstrahlung contribution and the coherent one, uncollimated and with a collimation of $U_c = 0.89$. Remind that $I = \frac{x}{\bar{\sigma}} \frac{dx}{d\sigma} = \frac{x}{\alpha^2 Z^2} \frac{dx}{d\sigma}$*

and energy) are shown in table 2.

$$\psi(\epsilon) = \begin{cases} 19.9 - 4 \ln \epsilon & \text{for } \epsilon \geq 0.88 \\ \sum_{n=0}^{5} e_n (0.88 - \epsilon)^n & \text{for } \epsilon < 0.88 \end{cases} \tag{20}$$

$$\text{with} \quad e_n = 19.7, 3.806, 31.84, 58.63, 40.77$$

For comparison of the simulated or analytical calculated intensities with the experimental one, not only the variable tagger bin width has to be considered but also multiple hits. They origin either from several electrons hitting the tagger focal plane detectors at the 'same time' or from one triggering several detectors if beeing scattered in a scintillator of the tagger ladder. This may be corrected by a so called multihit correction factor defined by $f_M = \frac{N_1}{N_1 + 2N_2 + 3N_3 + 4N_q}$ with N_n being the number of n hits in a row in the ladder, see figure 14

3.2 Collimation with non-ideal electron beam

The next step is to include collimation, but here in comparison to the previous chapter the effect of beam divergence, multiple scattering and a finite beam spot size was modelled. The beam spot effect translates into a 'fuzzy' collimator: instead of 'moving around' the beam, the same effect is achieved by 'moving around' the collimator by a lateral displacement $\delta r, \phi$ in polar coordinates. Due to a finite beam spot the collimator is no longer spherical symmetric with respect to the incident electron and the dependence of the

E_e	σ_x / y	$\sigma_{p_{x/y}}$	Di-Thickness	Colli dist.	Colli-radius
[MeV]	[mm]	[mrad]	[mm]	[m]	[mm]
855.0	0.2,0.06	0.08,0.08	0.1	2.5	1.5

Table 3: *Experimental parameters of the electron beam at MAMI used in the calculations presented here.*

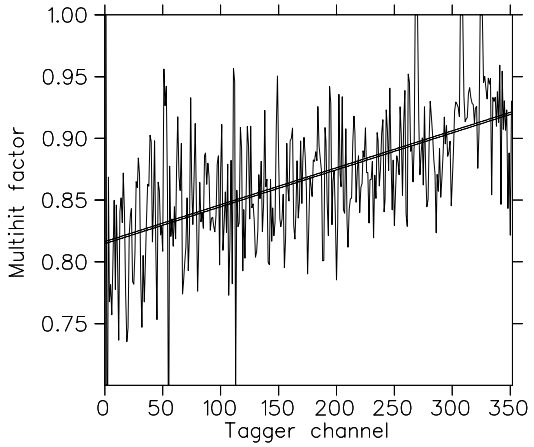

Figure 14: *Multihit correction factor f_M versus tagger channels*

collimator angle U_c on the collimator displacement has to be considered by a convolution of the intensity with the beam profile (compare with equation (13)):

$$I_{\bar{\rho}} = \int \rho d\rho \, d\phi \, g_s(\rho) \int_0^{u(\rho,\phi)} du \, I^{\mathrm{coh}}(x) \delta^D(u - u(x)) \tag{21a}$$

$$\text{with} \quad U_c^2 = U^2(\rho,\phi) + \rho^2 - 2U(\rho,\phi)\rho\cos\phi \tag{21b}$$

$$g_s(\rho) = \sigma_s^{-2} \exp -\frac{\rho^2}{2\sigma_s^2} \tag{21c}$$

The dependence of $u(x)$ on x is given in equation (15) and the function $u(\rho,\phi)$ is depicted in figure 15. A gaussian distribution for the angular displacement variation $\delta\rho = \delta r E_0/L$, stemming from the collimator displacement δr with distance L, is assumed. Due to the Heaviside function the ϕ integration is trivial and separates into the coherent intensity in terms of the Ψ_i functions and a collimation function $C_\sigma(U(x))$:

$$I_{\bar{\rho}} = I^{\mathrm{coh}}(x) C_\sigma(U(x)) \tag{22a}$$

$$C_\sigma(U(x)) = \int_{|U_c-U|}^{U_c+U} \rho d\rho \, g_s(\rho) \frac{1}{\pi} \arccos \frac{\rho^2 + U^2 - U_c^2}{2\rho U} + \Theta(U_c - U) \int_0^{U_c-U} \rho d\rho \, g_s(\rho) \tag{22b}$$

The ρ integration of the first term in (22b) is left as a numerical task while the second term gives: $\Theta(U_c - U)[1 - \exp(-(U_c - U)^2/2\sigma^2)]$. The function is

plotted in figure 15, whereas the effect of beam spot size, beam divergence and multiple scattering from (22b) on the lower energy part of a lattice vector peak, hence the part influenced by a collimator is shown in figure 16.

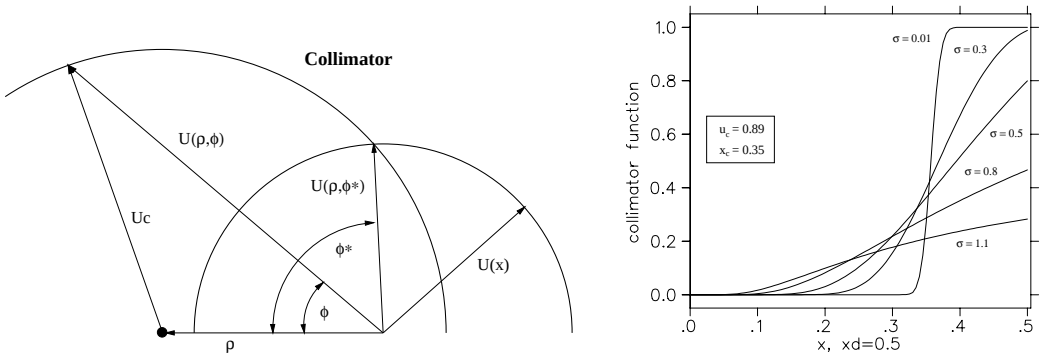

Figure 15: Left*: geometry of a displaced collimator (ρ beeing the polar displacement) resulting in equation (21b).* Right*: collimation function $C_\sigma(x)$ for various angle divergencies σ_s*

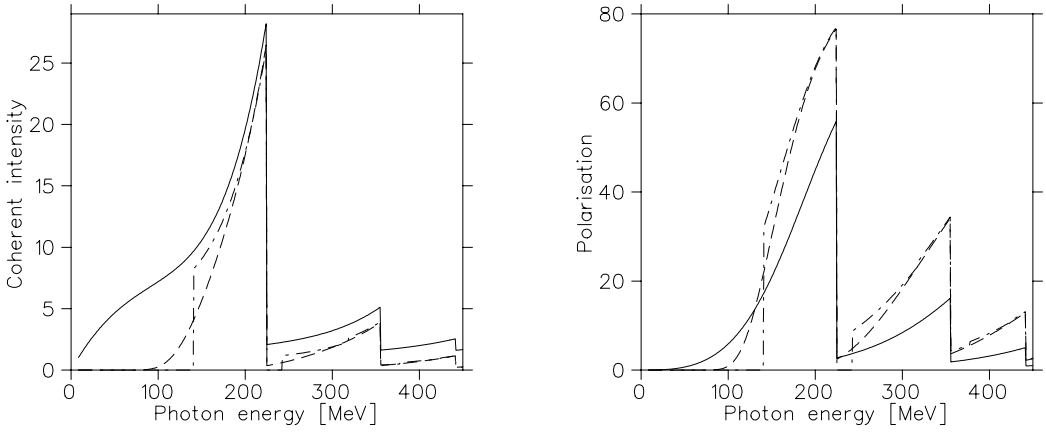

Figure 16: *Coherent intensity and polarisations and the result of collimation with and without a finite beam spot size and beam divergence in comparison with the uncollimated ones. Note, only equation (22) was applied, not (23a)*

The additional effect of the beam divergence is a variation of the crystal angles α_b, θ_b with respect to their mean values α, θ changing the intensity due the dependence of the lattice vectors on these angles. With the appropriate angle distribution functions derived via (23b) from the transversal momentum distribution function $g(\vartheta_b, \phi_b)$ of the beam yields after same trigonomet-

ric derivations:

$$I_d = \int \vartheta_b \, d\vartheta_b \, d\phi_b \, g_d(\vartheta_b, \phi_b) I_{\bar{\rho}}(\alpha_b, \theta_b) \tag{23a}$$

$$\text{with} \quad \theta_b = \sqrt{\theta^2 + \theta_b^2 - 2\vartheta_b \theta \cos\phi_b} \tag{23b}$$

$$\alpha_b = \alpha - \arcsin(\vartheta_b/\theta \cdot \sin\phi_b)$$

The distributions of the beam spot size $\sigma_{x/y}$ with the collimator at distance L and beam divergence $\sigma_{p_{x/y}}$ are approximated by spherical ones and appropriately convoluted which results in a quadratically adding of the deviations, to be used in equation (22b) and (23a):

$$\sigma_s^2 = \sigma_x \sigma_y / L^2 + \sigma_{p_x} \sigma_{p_y} \tag{24a}$$

$$\sigma_d^2 = \sigma_{p_x} \sigma_{p_y} + \bar{\sigma}_m^2 \tag{24b}$$

The effect of collimation on the incoherent part is described by the Hubbell cross section in case of an ideal beam. If a finite beam spot size and beam divergence come in to play equation (21) also applies for the photon angle differential intensity (17) which yields after integration where $v(\rho, \phi)$ is defined by (21b):

$$I_{\bar{\rho}}^{\text{inc}} = \int \rho d\rho \, d\phi \, g_s(\rho) I^{\text{inc}}(x, v(\rho, \phi)) \tag{25}$$

3.3 Multiple scattering

The last experimental influence to be regarded is the so called moliére scattering, meaning small angle scattering of the electrons in the radiator. In [Mol48] a polar angle distribution (gaussian with σ_m) of the electrons with respect to the incident momentum is derived. The involved observables shall be repeated here without further comment.

$$\sigma_m(s) = \frac{0.0246}{E_0^4 A^2} [Z^4 (Z+1)^4 \rho^2 s^2 - W(\Omega/s)] = a[bs^2 - W] \tag{26a}$$

$$\Omega = -1.32 \cdot 10^{-4} \frac{v_e A (1.13 + 3.76 \cdot (Z\alpha_{\text{em}}/v)^2)}{(Z+1) Z^{1/3} \rho}$$

$$l\bar{\sigma}_m = \int_0^l ds \, \sigma_m = a[bl^3/3 - W(\Omega/l) l + Ei(W(\Omega/l))\Omega] \tag{26b}$$

s/Ω is the mean number of elastic scattering in the target in depth s and W the Lambert's function and Ei the exponential integral which have to be

evaluated numerically. The radiator density is denoted by ρ and the incident electron velocity by v_e.

The influence of beam divergence and multiple scattering with respect to the lattice angles is dominant around the discontinuity and is shown for the collimated case [fig. 17] in comparison with the experimental data.

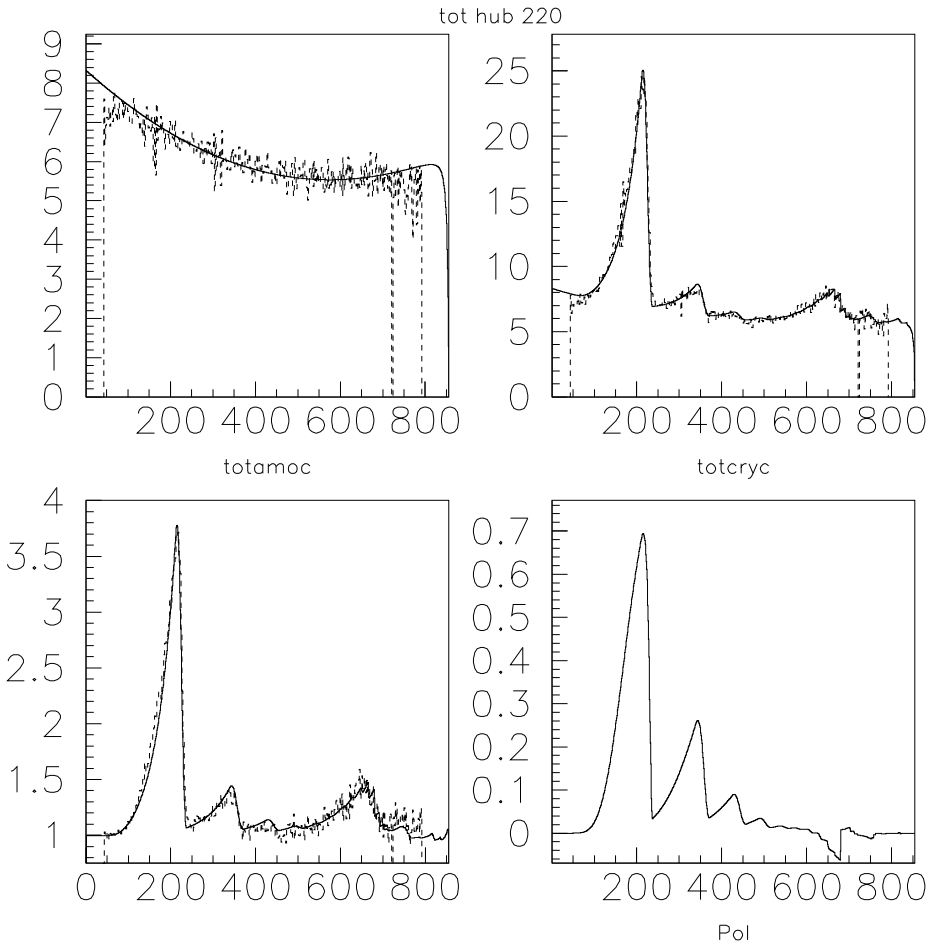

Figure 17: *Comparison between collimated analytic and experimental spectra for discontinuity at 220 MeV*

The relatively good fit of the analytical collimated relative cross section in the range x_c to x_d justifies the use of the calculated polarisation as a first estimate. It has to be noted, that this good agreement was only achieved

after increasing the MAMI beam divergence as given in table 3 by $\approx 3/4$, see also [tab. 7]. The intensity spectra calculated with the standard beam divergence would underestimate the smeared out fall off around the discontinuity of the measured spectra significantly. This fine tuning of the beam parameters was only possible through the comparison with the absolute total crystal intensities showing a higher sensitivity on beam parameters than the relative spectra and the use of a fast code like ANB . The average polarisation

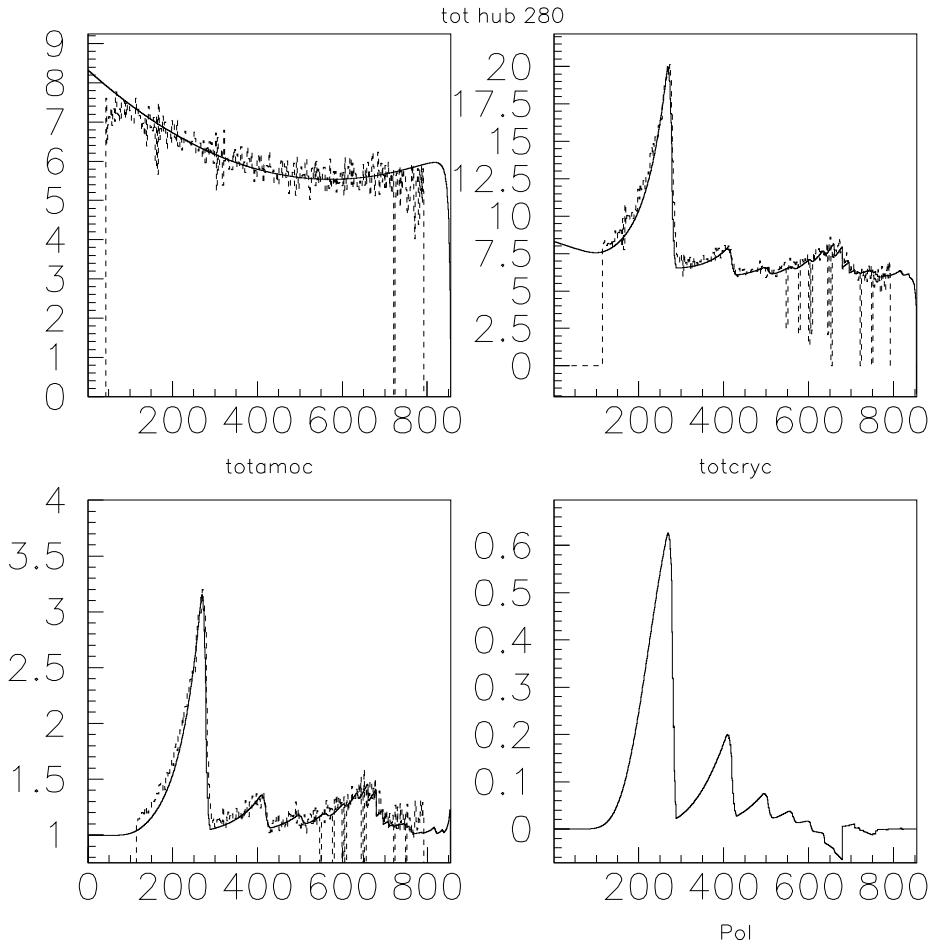

Figure 18: *Comparison between collimated analytic and experimental spectra for discontinuity at 280 MeV*

obtained with ANB , was calculated via

$$\bar{P}_{1/2} = \int_{x_{1/2}}^{x_d} dx\, \sigma^{\rm coh}(x) P(x) \Big/ \int_{x_{1/2}}^{x_d} dx\, \sigma^{\rm coh}(x) \tag{27}$$

whereas $x_{1/2}$ is defined as $P(x_{1/2}) = P(x_d)/2$, and $\bar{P}_c$ with the lower integration limit being the collimation cutoff x_c instead of $x_{1/2}$, is recorded in table 4.

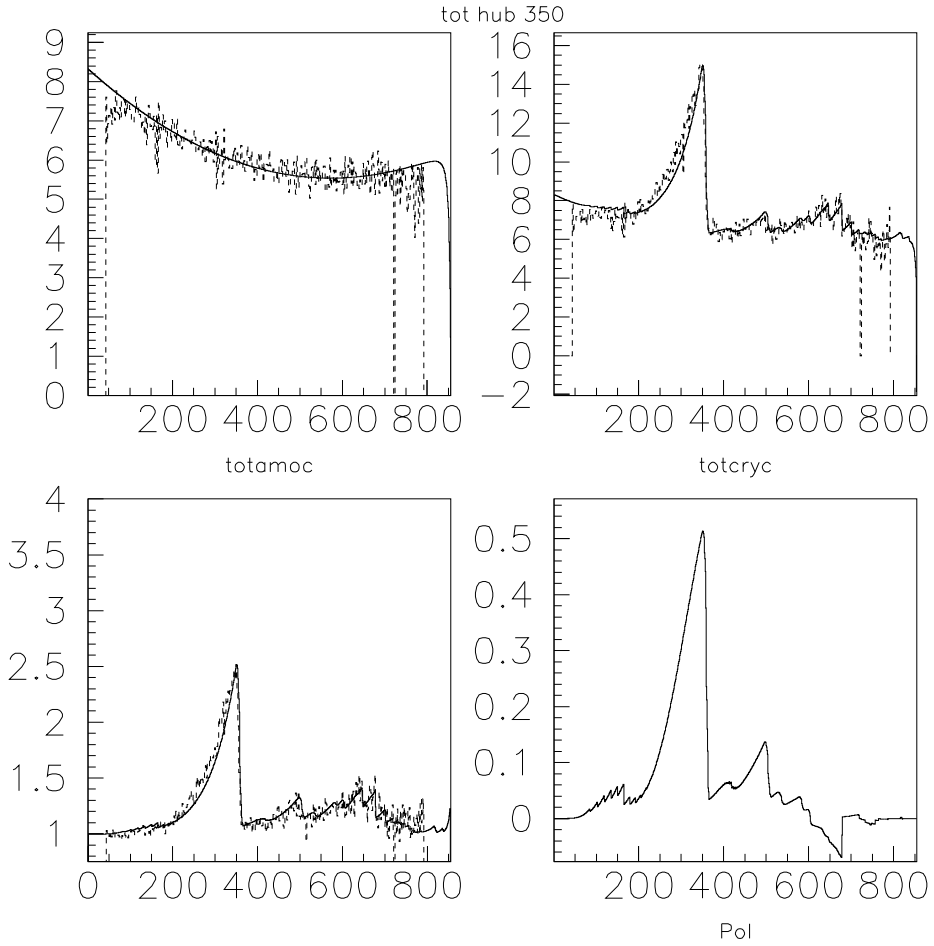

Figure 19: *Comparison between collimated analytic and experimental spectra for discontinuity at 350 MeV*

edge	(label)	[MeV]	220	280	350
crystal angles	α	[mrad]	0.694	0.662	0.600
	θ	[mrad]	0.0607	0.0607	0.0607
discontinuity	k_d	[MeV]	224.7	277.6	357.9
polarisation	$P_{\max}$	[%]	48	42	32
(uncollimated)	$P_{1/2}$	[%]	24	21	16
	$\bar{P}$	[%]	38	32	24
photon energy	$k_{\max}$	[MeV]	210	266	346
	$k_{1/2}$	[MeV]	159	207	280
polarisation	$P_{\max}$	[%]	70	64	54
(collimated)	$P_{1/2}$	[%]	36	32	27
	$\bar{P}$	[%]	58	52	42
photon energy	$k_{\max}$	[MeV]	212	266	346
	$k_{1/2}$	[MeV]	159	205	280

Table 4: *Mean polarisation (27) and properties of the bremsstrahlung for three different diamond settings, applied in the ^{4}He experiment.*

4 Debye Waller factor

The so-called Debye Waller factor (31a) governs the ratio of incoherent to coherent contribution to the total bremsstrahlung cross section and is only necessary for a crystal radiator, which means that the incoherent cross section employing a crystal instead of an amorphous radiator differs non trivial. It depends on the momentum transfer to the lattice and has to be multiplied to the 4 fold differential cross section, which effectively leads to a modified form-factor. Now the analytical integration of the Bethe-Heitler cross section to obtain the Hubbell one is no longer feasible and a different method to account for the Debye Waller factor needs to be applied. The following two chapters deal with two different approaches to that problem.

4.1 Reduction factor

The effect of the Debye Waller factor is effectively taken care of by a reduction factor r_D depending only on the photon energy [fig. 22] which has to be multiplied to the Hubbell intensity: $I^{\text{inc}}_{\text{Hub}}=r_D I^{\text{amo}}_{\text{Hub}}$. It has to be noted, that the screening constant used for $I^{\text{amo}}_{\text{Hub}}$ was calculated via the method described in section 4.2 and evaluates with the ^{12}C realistic form-factor [fig. 23] to $C_{\text{amo}} = 90.8$. This constant was also calculated in a Thomas Fermi model [Hub58]

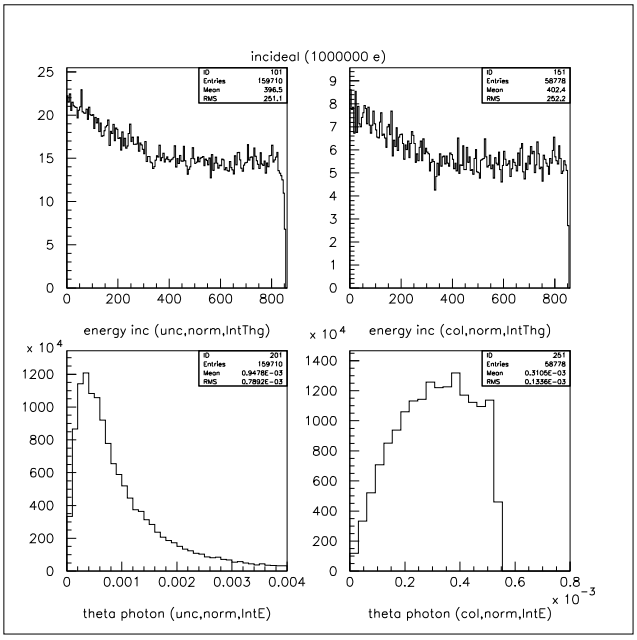

Figure 20: *Incoherent (uncollimated and collimated) intensities from MCB for an ideal electron beam and their angular distributions of the emitted photon in the lab system.*

yielding $C = 111$, whereas Timm [Tim69] suggests $C = 71$ for carbon. This reduction factor has only to be calculated once via a numerical integration to yield a table for interpolation or to be modelled by a fit function:

$$r_D(x) = \int d\vartheta_\gamma d\vartheta_e d\phi \, I^{\mathrm{BH}} \left(1 - f_D(q^2)\right) \Big/ \int d\vartheta_\gamma d\vartheta_e d\phi \, I^{\mathrm{BH}} \tag{28}$$

were the Bethe Heitler intensity (BH) is given by [BeH 54]:

$$\begin{aligned} \frac{d^3 I^{\mathrm{BH}}}{d\vartheta_e d\vartheta_\gamma d\phi} &= \frac{s_e s_\gamma}{2\pi E_0^2 p_0^2 q^4} F^2 \\ &\times \left\{ \frac{s_e^2}{(1-x-c_e)^2}(4-q^2) + \frac{s_\gamma^2}{(1-c_\gamma)^2}\left(4(1-x)^2 - q^2\right) \right. \\ &\left. -2\frac{s_e s_\gamma \cos\phi}{(1-x)(1-c_\gamma)}\left(4(1-x) - q^2 + 2x^2\right) + 2x^2 \frac{s_e^2 + s_\gamma^2}{(1-x-c_e)(1-c_\gamma)} \right\} \end{aligned} \tag{29}$$

$$q^2 = p_0^2 + p^2 + x^2 + 2x\left(c_e - c_\gamma\right) - 2\left(c_\gamma c_e + s_\gamma s_e \cos\phi\right) \tag{30}$$

The incident and scattered electron momentum is denoted as p_0 and p respectively with the momentum transfer q, here in units of E_0. $F(q^2 E_0^2)$ is the

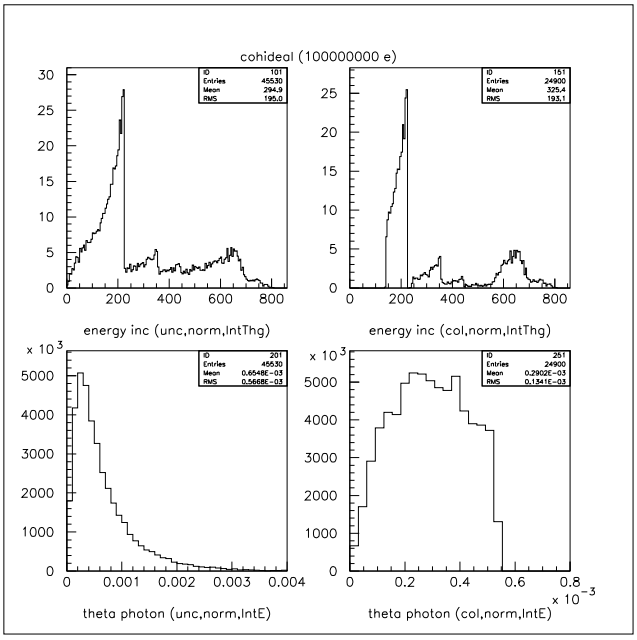

Figure 21: *Coherent intensities and angular distributions from MCB for ideal beam.*

atomic form-factor and f_D the Debye Waller factor. ϑ_e and ϑ_γ are the polar angles of the electron and photon and ϕ the azimuthal angle between both momenta. The following abbreviations and relations are employed:

$$f_D = \exp(-Aq^2 E_0^2) \qquad A = 101.48 \quad \text{at room temperature} \tag{31a}$$

$$c_\gamma = p_0 \cos\vartheta_\gamma \qquad s_\gamma = p_0 \sin\vartheta_\gamma \tag{31b}$$

$$c_e = p \cos\vartheta_e \qquad s_e = p \sin\vartheta_e \tag{31c}$$

$$p_0^2 = 1 - E_0^{-2} \qquad p^2 = (1-x)^2 - E_0^{-2} \tag{31d}$$

f_D depends weakly via a function $A(T_{\text{Debye}}, T_{\text{Room}})$ on room and Debye temperature, with a typical value given in (31a). The numerical integration was performed via an adaptive Monte Carlo method called VEGAS [NRe92], with the requirement of statistical accuracy of less than 10^{-3}. For room temperature the resulting reduction factor can be well described by the following parametrisation:

$$r_D(x) = a_1 + a_2/(1 - a_3 x) \qquad a_i = 0.7435, .0043, 0.9863 \tag{32}$$

The residual deviations of the numerical calculation compared to the fit are in the order of 1% with $\chi^2_{\text{rel}} = 0.02$ and it may be deduced from figure 22 that they are statistically only.

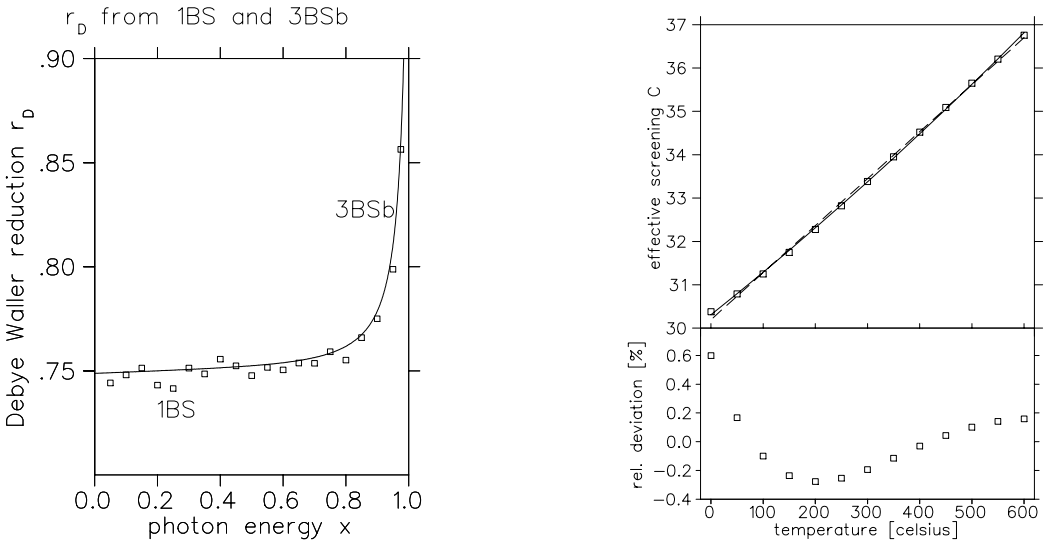

Figure 22: *Left: Debye Waller reduction factor $r_D(x)$. Shown is the fit (32) to the numerical calculations (circles) of equation (28). Right: Debye Waller effective screening constant. Plotted are the curves for C_{eff} with a quadratic and linear fit and the deviation of the numerical results to the latter one.*

4.2 Effective screening

The second method is based on the idea of an effective form-factor. For the Hubbell cross section a dipole form factor with the screening constant C is used which has to be modified by the Debye Waller factor. Its influence on the form-factor is a suppression of lower q-values for the incoherent cross section. Although the description of the modified form-factor via a dipole form-factor with effective screening constant $F^2_{C^{\text{eff}}} \sim (1 - f_D)F^2_C$ seems unsatisfactory [fig. 23], it is to emphasise that the q^2 dependence of the cross section is much less important than its integral. From a comparison of the total cross section calculated from a numerical integration of the Bethe Heitler cross section employing the Debye Waller factor (see equation (28)) and the ^{12}C realistic form-factor [Ram95] with the numerical integrated Hubbell cross section an effective screening parameter C_{eff} for the latter one is determined via a fitting procedure. This was done for a finite temperature range. The resulting screening constants in dependence of the temperature were linear fitted giving:

$$C_{\text{eff}}(T) = a_1 + a_2 T \qquad a_i = 27.24, 0.0108 K^{-1} \tag{33}$$

Incoherent ANB spectra calculated with both methods show a relative deviation of less than 2% over the hole energy range. Therefor it can be deduced

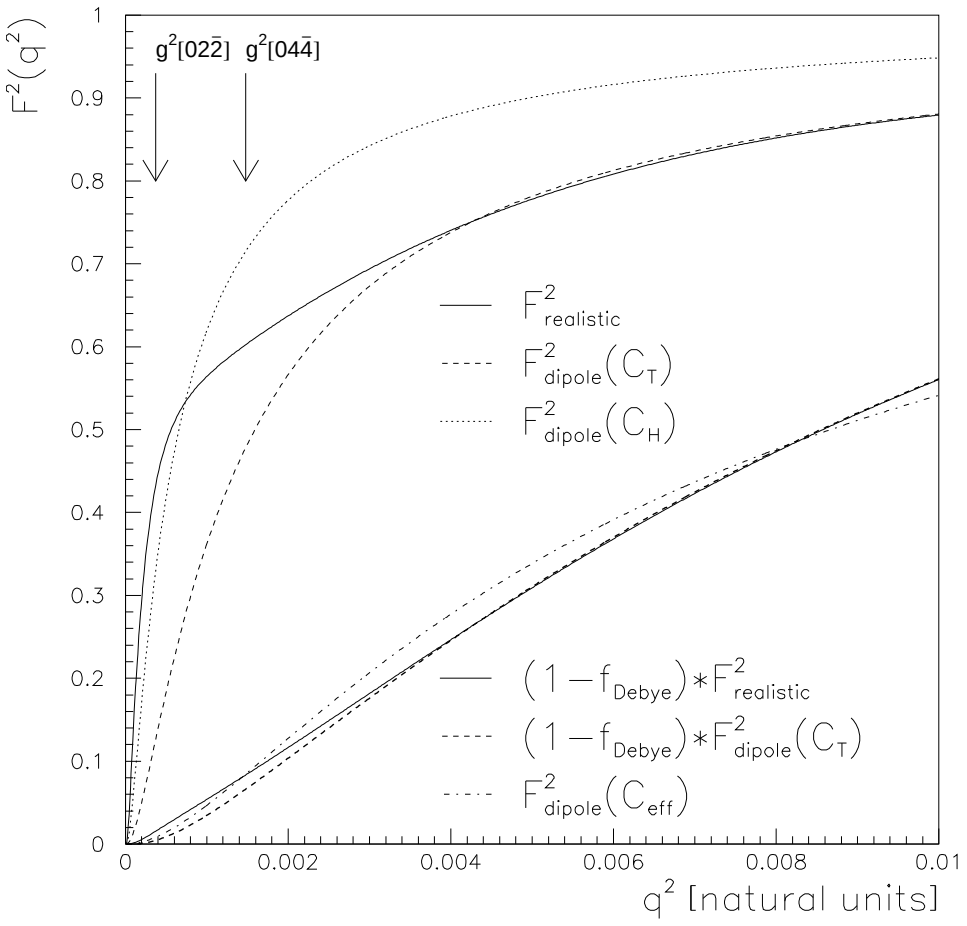

Figure 23: *The ^{12}C realistic form-factor from [Ram95] is compared with the dipole form-factor applying a screening constant of $C_H = 111$ from a Thomas-Fermi model [Hub58] and $C_T = 71$, suggested by Timm [Tim69]. To model the effective form-factor $F^2_{eff}(q^2) = (1-f_D)\ F^2_{realistic}$, an effective dipole form-factor with a temperature dependend screening constant $C(T)$, see equation (33), was used.*

that these methods are valid treatments of accounting the debye waller factor employing the hubbell cross section. Furtheron the effective screening method is used because the temperature dependence of the Debye Waller factor is easier implemented there. The systematic error introduced by these treatments may be estimated by their relative deviations giving a systematic error for the polarisation of less than one per cent point absolute in the maximum of the polarisation and much smaller elsewhere.

4.3 Adaption to MCB

For the Monte Carlo description via MCB the same methods were used but had to be adapted to a two fold differential (in photon energy x and angle ϑ) treatment. Here, the basis of the modeling of the incoherent Hubbell intensity consists of equation (17) and (33) for the effective form-factor method or a two dimensional reduction factor $r_D(x,\vartheta)$ in the other case:

$$r_D(x,\vartheta) = \int d\vartheta_e d\phi\, I^{\mathrm{BH}} \left(1 - f_D(q^2)\right) \Big/ \int d\vartheta_e d\phi\, I^{\mathrm{BH}} \tag{34}$$

This was performed numerically using a grid for the photon variables, i.e. 48 steps in photon energy and 18 in the reduced photon angle $U = \vartheta/E_0 \in [0, 1.9]$. This table was then fitted employing three different fit functions, given in equation (35a) with their parameters in table 5 and their plots in [fig. 24].

$$r_D^{(1)}(x,\vartheta) = (p_1 + p_2 e^{p_3 x}) \left(p_4 + p_5\vartheta + p_6\vartheta^2\right) \tag{35a}$$

$$r_D^{(2)}(x,\vartheta) = \left(p_1 + p_2\vartheta + p_3\vartheta^2\right) \left(p_4 + (1 - p_5 x)^{-1}\right) \tag{35b}$$

$$\begin{aligned} r_D^{(3)}(x,\vartheta) = {} & p_1 + p_2(p_3 - x)^{-p_4} + \left[p_5 + p_6 / \left(1 + p_7(p_8 - x)^2\right)\right] \\ & \times \left\{1 - \exp\left[\left(p_9 + p_{10}/(1 + p_{11}(p_{12} - x)^2)\right)\vartheta\right]\right\} \end{aligned} \tag{35c}$$

Although fit no. 3 has the lowest χ^2, $r_D^{(1)}$ was taken for further calculations due to the smaller computing consumption in MCB .

5 Resulting polarisation

For an estimate of the systematic error of the polarisation, two sources were considered: the one introduced by the two methods described above and the consequences of the uncertainty of the MAMI beam parameters, see table 3.

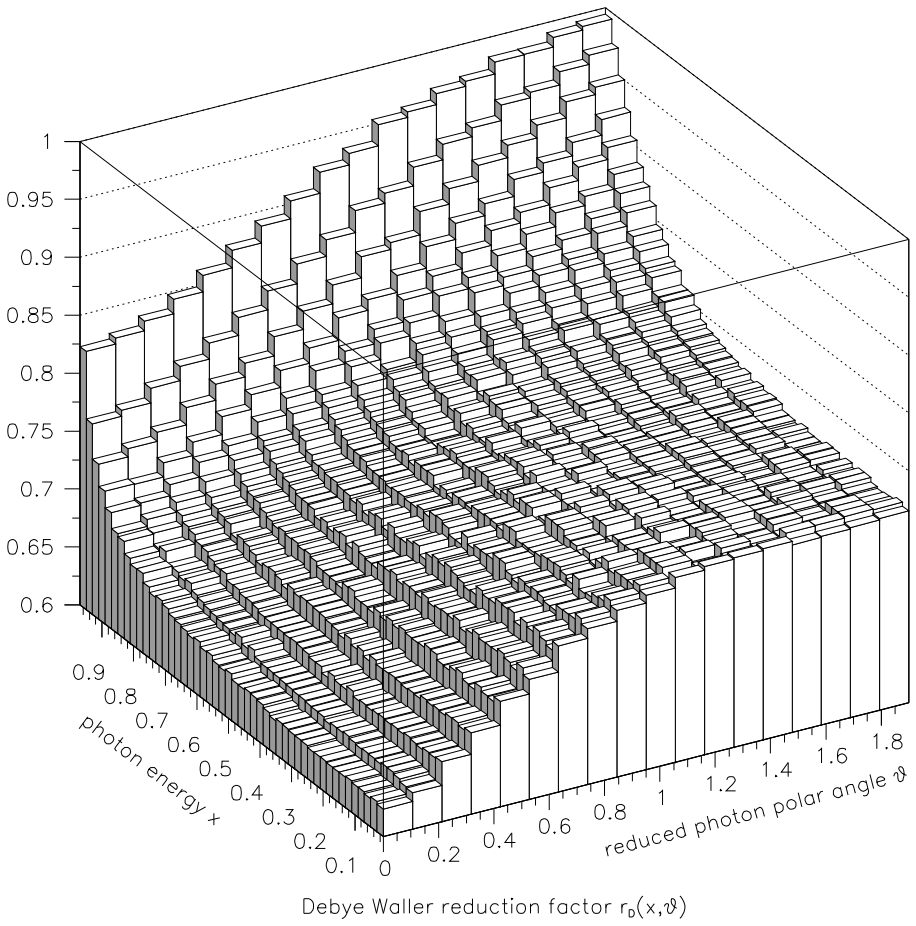

Figure 24: *Debye Waller reduction factor $r_D(x, \vartheta)$ in photon energy x and angle ϑ for MCB . The numerical calculation of equation (34) was done using an adaptive Monte Carlo integration method called VEGAS, see [NRe92], which therefor shows small fluctuations.*

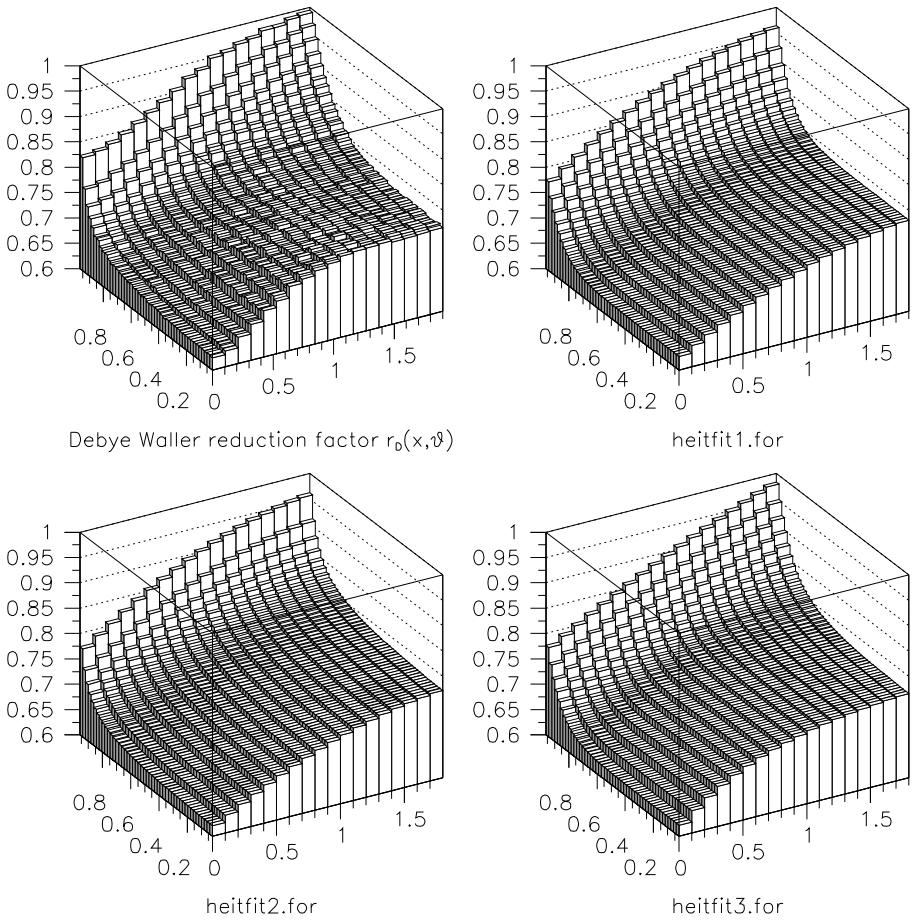

Figure 25: *Two dimensional fits to Debye Waller reduction factor $r_D(x,\vartheta)$ in photon energy x and angle ϑ for MCB . Panel upper left shows again the numerical calculation whereas the other panels are the three fits, where the functions and parameters are given in equation (35a) and table 5, respectively.*

fit	1	2	3		3
p_1	0.664203	0.0103543	0.609626	p_7	103.549
p_2	4.09235E-06	0.00262039	0.538128	p_8	0.909567
p_3	11.1074	-0.000621878	2.05571	p_9	-1.6652
p_4	0.932192	58.1925	12.1215	p_{10}	1.43357
p_5	0.237098	0.985096	0.16191	p_{11}	12.8126
p_6	-0.0564868		0.46922	p_{12}	0.901264
χ^2	1.070E-04	0.1296E-03	0.4938E-04		

Table 5: Parameters of fits in equation (35a) to the two dimensional Debye Waller reduction factor (34)

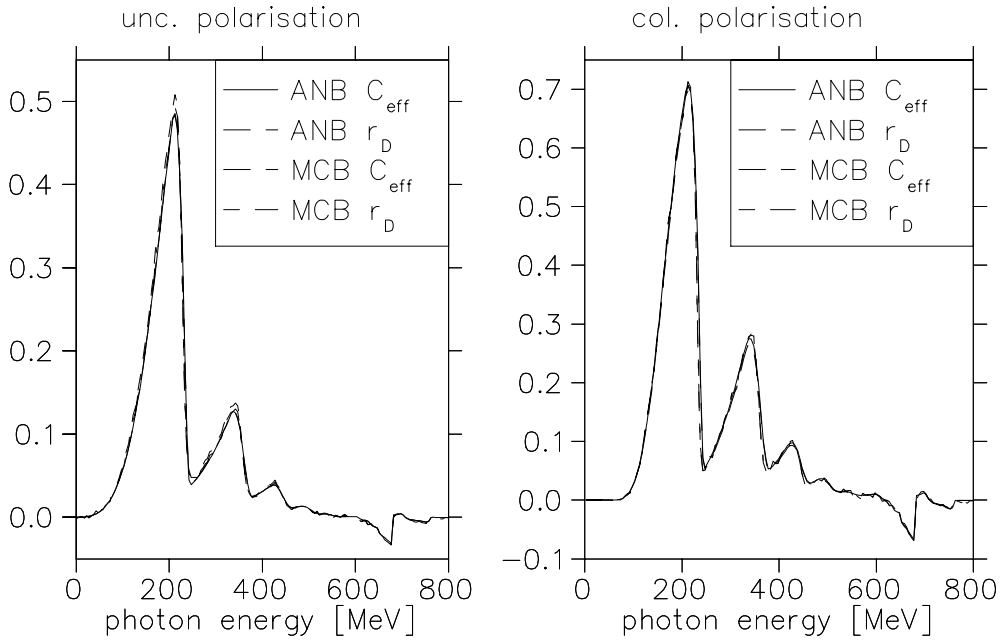

Figure 26: *Compared are the uncollimated* (left) *and collimated* (right) *polarisations from MCB and ANB for the two methods. Note that the r_D method in MCB somewhat overestimates the polarisation in the peaks.*

In order to derive a systematic error from the uncertainty of the beam parameters, the effect of all experimental effects as beam divergence, finite beam spot size, diamond temperature, multiple scattering on the polarisation would have to be studied. But for an appropriate estimate only a variation of the beam divergence having the biggest impact on the polarisation was used. The polarisation was calculated for a 20% higher and lower beam divergence and in reagard of its monotonically dependence a photon energy dependent error, denoted with (BD), could be derived via (36a). The difference in the degree of polarisation is about 0.02 with collimation in the $[02\bar{2}]$ peak and much less elsewhere. A more detailed overview on the systematic error is given in table 6.

Also the influence on the polarisation of the two methods to deal with the Debye Waller factor, as described in section 4, with their implementation in ANB and MCB , was investigated to have an estimate of this error, see (36b). The differences of the effective form-factor method and the reduction factor method for the collimated case is less than 0.02 for both codes and again the highest discrepancy was found to be in the peak region.

$$\Delta P_{\mathrm{BD}}(x) = |P_{.8\mathrm{BD}} - P_{1.2\mathrm{BD}}|/2 \tag{36a}$$

$$\Delta P_{\mathrm{C,r}}(x) = |P_{C_{\mathrm{eff}}} - P_{r_D}|/2 \tag{36b}$$

$$\Delta P_{\mathsf{ANB\ MCB}}(x) = \langle\, |P_{\mathsf{ANB}} - P_{\mathsf{MCB}}|/2 \,\rangle_{\mathrm{C,r}} \tag{36c}$$

The overall very good agreement of these both methods indicate their reliability, although there is one exception: The two dimensional reduction factor for MCB seems to overestimate the polarisation in the uncollimated case by a factor of 1.07, compare [tab. 6] in the peak region (but much less elsewhere). Therefore and due to the fact that the temperature dependence is easier implemented in that method the effective form-factor method was choosen as the optimal method to model the effect of the Debye Waller factor in the incoherent contribution. The photon energy dependent errors calculated via equations (36) were added absolutely to a total systematical error and plotted with the polarisation in figure 29 and 30. The polarisations for all three discontinuities with their systematic errors are recorded in ascii files (pol96_{220,280,350}.dat) attached to this report. Their format consists of four columns: the first beeing the photon energy followed by the coherent intensity, the degree of polarisation and the total systematic error. The photon energy values correspond to the Glasgow tagger channels.

In order to complete the survey of the errors involved, the influence of all experimental parameters X, like crystal angle (α), beam spot size ($\sigma_s^{x,y}$), beam divergence ($\sigma_p^{x,y}$), diamond thickness (d_{rad}) and collimation angle (here:

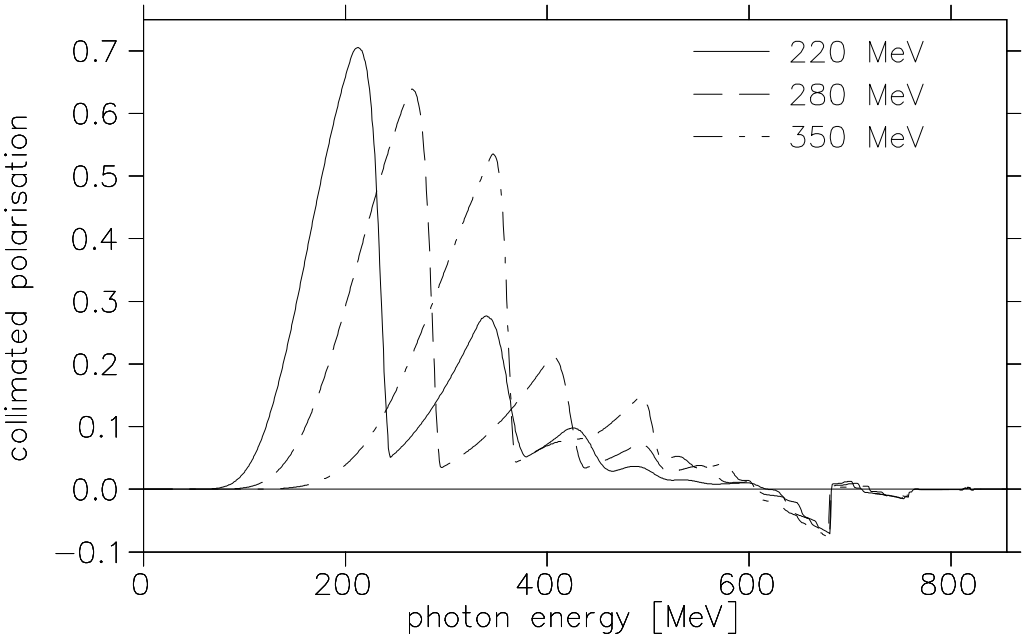

Figure 27: *Plotted are the collimated polarisations for the three crystal angle settings, see table 4, for comparison.*

	absolute difference in polarisation			
	uncollimated		collimated	
	mean	$[02\bar{2}]$ peak	mean	$[02\bar{2}]$ peak
ΔP_{BD}	$1 \cdot 10^{-3}$	0.01	0.01	0.02
$\Delta P_{\mathrm{C,r}}$(ANB)	$4 \cdot 10^{-4}$	$2 \cdot 10^{-3}$	$3 \cdot 10^{-3}$	0.01
$\Delta P_{\mathrm{C,r}}$(MCB)	$5 \cdot 10^{-3}$	0.03	$5 \cdot 10^{-3}$	0.02
$\Delta P_{\mathrm{ANB\ MCB}}$	$4 \cdot 10^{-3}$	0.02	$6 \cdot 10^{-3}$	0.01

Table 6: *Overview of systematic error of the polarisation due to uncertainty in the MAMI beam parameters and the methods dealing with the Debye Waller factor. The error in the peak is always the maximal error and 'mean' shows the averaged systematic error over the whole energy range.*

X_i	X_i^0	units	$r_c = 1.5$	2.5	4	uncollimated
ϑ	.0607	rad	0.18	0.19	0.19	0.18
α	.694	rad	1.18	1.33	1.43	1.5
$\sigma_s^{x,y}$	.2,.06	mm	0.003	0.002	0.001	0
$\sigma_p^{x,y}$	.16,.16	mrad	0.047	0.013	0.007	0.007
d_{rad}	.1	mm	0.071	0.02	0.004	0.005
d_c	2.5	m	0.11	0.17	0.09	0

Table 7: *Variation of polarisation E_X (37) in dependence of parameter X_i for three different collimators (r_c) and the uncollimated situation.*

collimator distance d_c) on the degree of polarisation was investigated. For a calculation of the error propagation of those parameters

$$\frac{\Delta P}{P_0}(X_i) = \left|\frac{\partial \bar{P}}{\partial X_i}\frac{X_i^0}{P_0}\right| \frac{\Delta X_i}{X_i^0} = E_X \frac{\Delta X_i}{X_i^0} \tag{37}$$

the slope $\partial\bar{P}/\partial X_i$, where $\bar{P}$ is defined in (27), was determined by computing the polarisations $\bar{P}(X_{ij})$ from ANB for excessive and reduced parameters $X_{ij} = X_i^0(1 \pm \epsilon_j)$ with $\epsilon_j = 0, .01, .02, .04, .06, .08, .1$, see figure 28. The polarisations in dependence of ϵ_j were fitted with a second order polynomial and its slope taken as the slope of the error propagation of this particular parameter X_i while the others were kept to their standard values X_i^0. From that E_X can be derived and is recorded in table 7 for four different collimators. One can deduce from the table that the biggest effect arise from the diamond thickness, crystal angle α and beam divergence, wereat the latter two have the larger uncertainties. Asuming an error in beam divergence of 20% (one sigma) the error propagation for the polarisation gives a difference ΔP in the degree of polarisation of about 1% absolute, which is consistent with the error estimate on page 37.

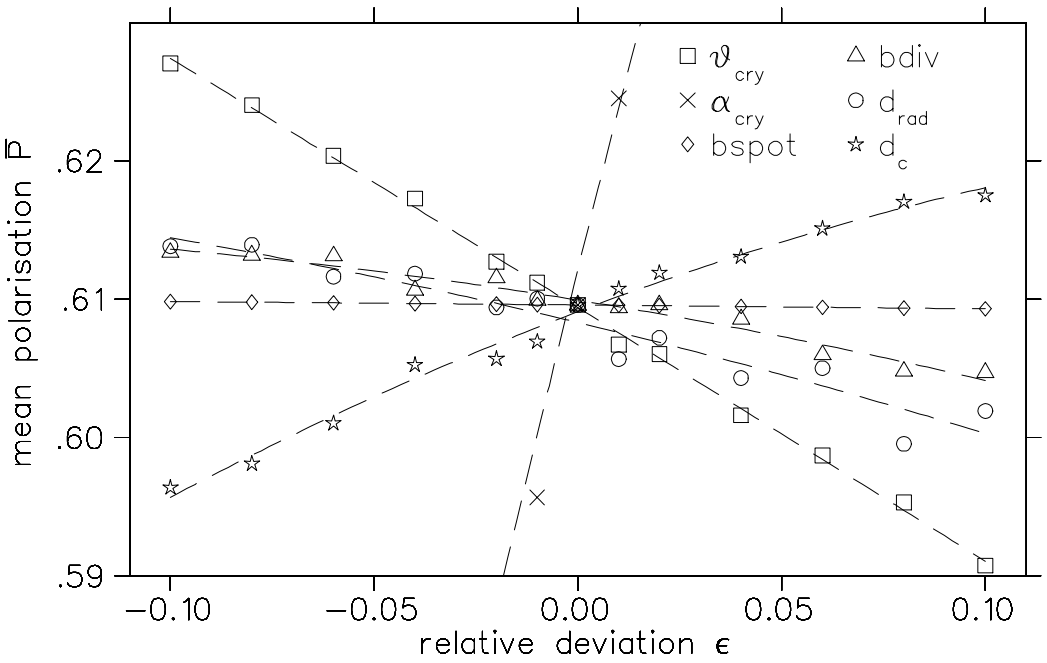

Figure 28: *Mean polarisations with a $r_c = 1.5$ mm collimator for all six parameters X_i versus the relative deviations ϵ_j with their fit of a second order polynom to deduce the variation E_X at X^0.*

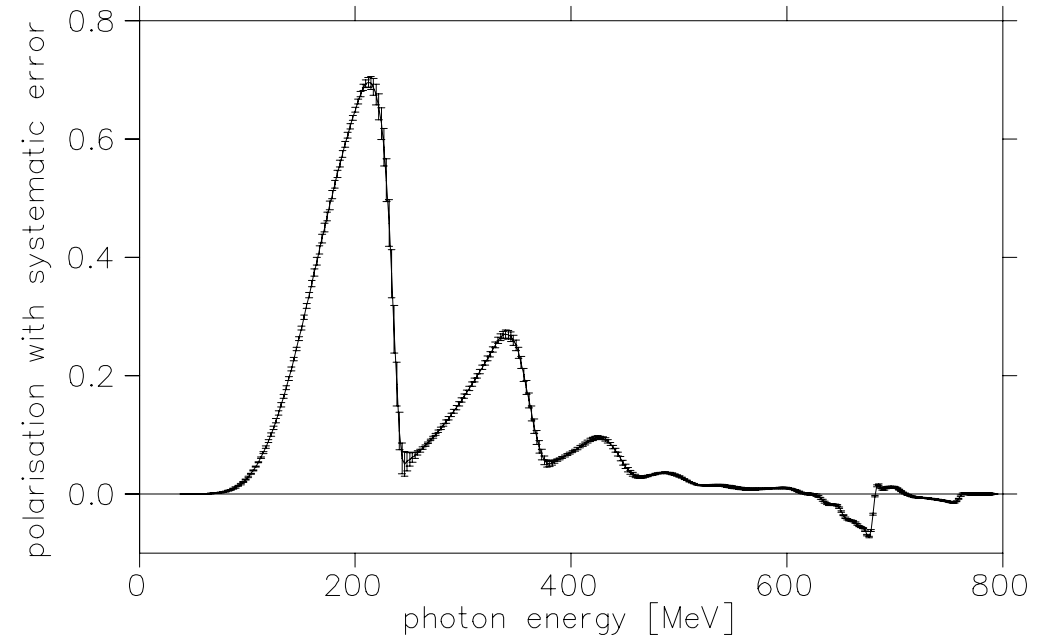

Figure 29: *Resulting collimated polarisation for discontinuity at 220 MeV and the systematic error from (36a) and (36b).*

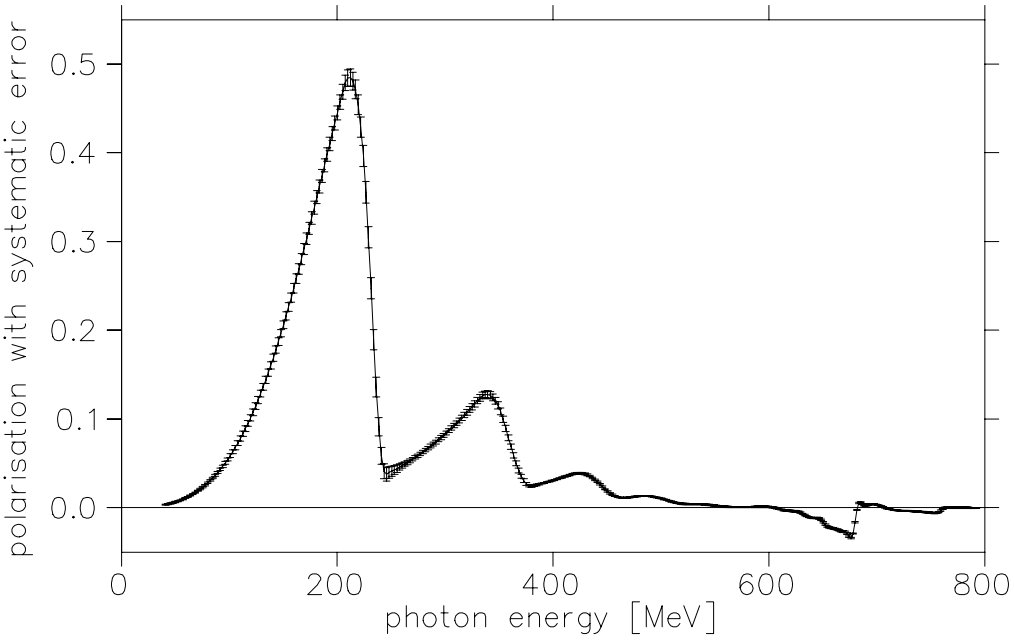

Figure 30: *Same as figure 29 but for the uncollimated case.*

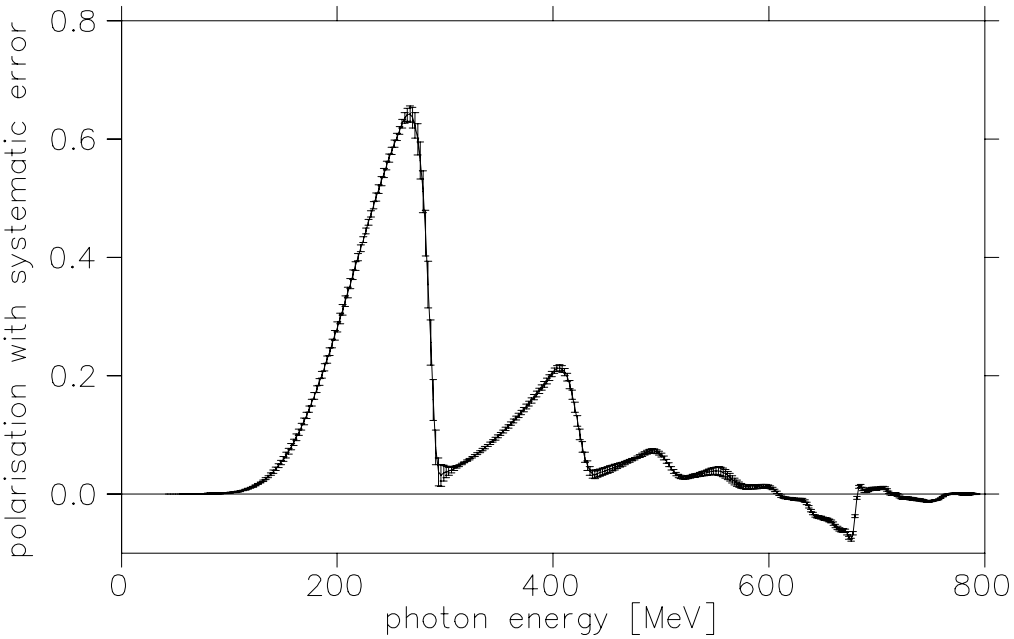

Figure 31: *Resulting collimated polarisation for discontinuity at* 280 *MeV.*

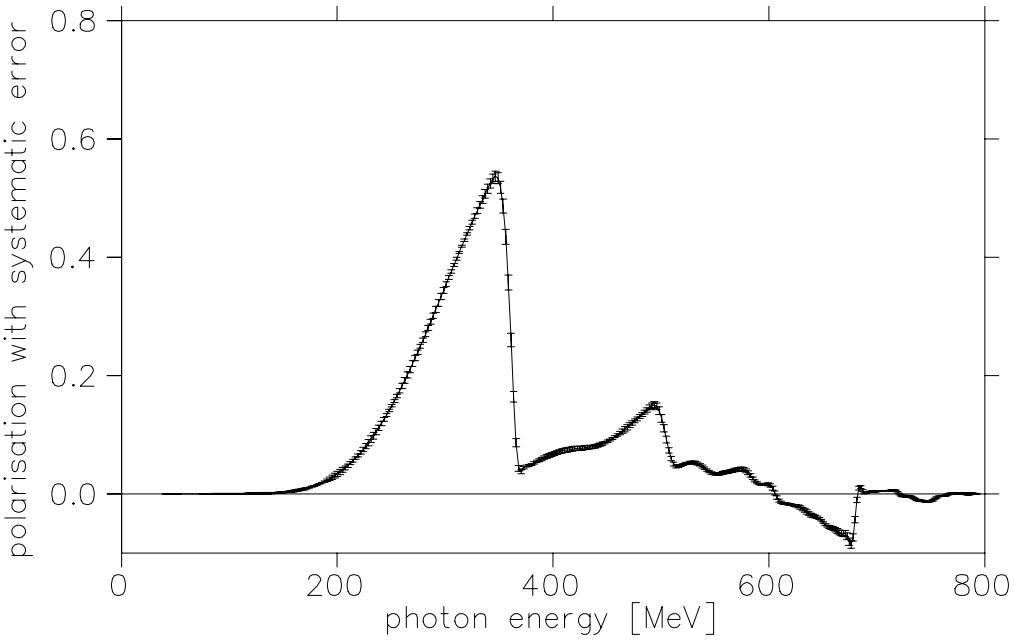

Figure 32: *Resulting collimated polarisation for discontinuity at* 350 *MeV.*

References

[BeH 54] W. Heitler, The Quantum Theory of Radiation (1954), Clarendon Press, Oxford.

[Bjø64] J. D. Bjørken and S. D. Drell, Relativistic Quantum Mechanics (1964). Mc Graw Hill, New York.

[Bol62] G. Bologna, Il Nuovo Cimento 48 (1967) 756

[Dia68] G. Diambrini Palazzi, Rev. Mod. Phys. 40 (1968) 611

[Hal84] F. Halzen and A. D. Martin, Quarks & Leptons (1984). John Wiley & Sons, Inc.

[Loh94] D. Lohmann, M. Schumacher et al., Nucl. Instr. and Meth. A 343 (1994) 494
D. Lohmann, Diploma Thesis 1992, II Physikalisches Institut, Georg-August-Universität Göttingen

[May51] M. M. May, Phys. Rev. 84 (1951) 265

[NRe92] Numerical Recipes in C, W.H. Press, S.A. Teukolsky, W.T. Vetterling, B.P. Flannery, Cambridge University Press

[Ram95] F. Rambo, Diploma Thesis 1995, II Physikalisches Institut, Georg-August-Universität Göttingen

[Tim69] U. Timm, Coherent Bremsstrahlung of Electrons in Crystals, Fortschritte der Physik 17 (1969) 765

[KoM59] H.W. Koch and J.W. Motz, Bremsstrahlung Cross-Section Formulas and Related Data, Rev. Mod. Phys. 31 (1959) 920

[MOw73] J.L Matthews and R.O. Owens, Accurate Formulae for the Calculation of high Energy Electron Bremsstrahlung spectra, Nucl. Instr. Meth. 111 (1973) 157

[Mol48] G. Moliére, Z. Naturforschung 3a (1948) 78

[Hub58] J.H. Hubbell, Spectrum of thin Target Bremsstrahlung bounded by a forward circular Cone, J. Appl. Phys., Vol. 30, No. 7 (1959) 981

[Wun97] S. Wunderlich, Simulation of Experimental and Apparative Influences on the Coherent Bremsstrahlung, Internal Report 97/1